2014

The doubly-fed induction generator in the rotor-tied configuration

Nicholas David
Iowa State University

The doubly-fed induction generator in the rotor-tied configuration

by

Nicholas Adam David

A thesis submitted to the graduate faculty

in partial fulfillment of the requirements for the degree of

MASTER OF SCIENCE

Major: Electrical Engineering

Program of Study Committee:

Dionysios Aliprantis, Major Professor

Venkataramana Ajjarapu

James McCalley

Umesh Vaidya

Iowa State University

Ames, Iowa

2014

TABLE OF CONTENTS

LIST OF TABLES

LIST OF FIGURES

ACKNOWLEDGMENTS

I would like to express my gratitude to those who have helped me accomplish this work, shared their knowledge, and inspired me along the way. A special thank you to my major professor, Dr. Dionysios Aliprantis, for all of his support. His shared knowledge of power electronics and electric machines, and guidance in conducting experiments and analyses has played a vital role in this work. Without his assistance, I would not be at the point I am in my graduate research.

I would also like to thank my committee members, Dr. James McCalley, Dr. Umesh Vaidya, and Dr. Venkataramana Ajjarapu. Their knowledge and insight of electrical power systems and controls is greatly appreciated, and has me considering other interesting topics. Additionally, I would like to thank Dr. Xiaomin Kou for introducing me to the world of power electronics and the opportunities he provided.

ABSTRACT

The demand for electricity from renewable sources continues to rise, and with it, the need for more efficient wind energy conversion systems. Wind turbines equipped with a wound-rotor induction machine can be operated in a more efficient configuration than currently popular, with little to no change in system hardware. By coupling the machine to the grid inversely to the norm, losses in the system can be reduced. The theory describing this configuration and mode of operation is detailed, with steady-state operating conditions calculated. Theoretical analysis shows that core loss due to magnetic hysteresis can be reduced, and efficiency increased. Operation in the proposed configuration is compared experimentally to the conventional one, with results indicating a substantial improvement of energy-conversion efficiency for the machine under test. Losses associated with the electronic power converters and auxiliary hardware are not expected to change significantly, and are not considered.

CHAPTER 1. INTRODUCTION

The global wind streams provide a renewable source of energy, arising from global temperature variations. In response to the variability of wind speeds for a particular location, variable-speed wind energy conversion systems (WECS) have been developed [1], [2]. Horizontal-axis wind turbines are the most popular form in commercial use. These turbines typically rely on a wound-rotor induction machine as the means of electromechanical energy conversion. The machine is usually configured so that the stator terminals are connected to the grid, and the rotor terminals connected to an electronic power converter; this is the Type-3 topology, called the doubly-fed induction generator (DFIG).

Using a DFIG offers the flexibility of variable speed operation, while allowing full control of the electromagnetic torque production. This makes them effective in extracting the maximum amount of power across a range of wind speeds. These WECS are usually designed so that the electronic power converter handles one third of the total power at the rated wind speed, which corresponds to a specific operating speed range. In general, the energy conversion efficiency of these systems varies with wind speed. At operating speeds below the synchronous speed, circulating currents within the machine lead to increased ohmic losses. Since magnetic hysteresis losses [3] are frequency dependent, the variable nature of the rotor current frequency leads to changes of core loss at different speeds. When the DFIG is in the conventional stator-tied configuration, the stator core is magnetized at the grid frequency, and the rotor core is magnetized at a frequency less than half of this. The amount of hysteresis loss in the stator core is nearly constant, while the hysteresis loss in the rotor core is variable, and goes to zero at synchronous speed.

Motivation For Improvement

For many reasons, it is desirable to increase electrical energy generation from renewable energy resources, particularly wind. One approach to achieve this is to simply build and install more wind turbines to capture the wind resource over a larger geographic range. Another method is to increase the radius of swept area for each turbine, thereby extracting energy from a larger volume of air. Both of these methods require additional resources and material costs. In this thesis, the aim is to increase the efficiency of energy conversion, which will result in more energy delivered to the electrical power system for the same amount of installed infrastructure and energy extracted from the wind resource.

While studying the principles of operation regarding DFIGs, the question of why we configure the DFIG in the way we do arises. Traditionally, the DFIG is configured with the stator windings connected to the grid, thereby inducing a magnetic field in the stator core that varies sinusoidally with the grid frequency. The magnetic field in the rotor core is controlled by the electronic power converter to generate a specific amount of torque and remain synchronized with the magnetic field in the stator core [4].

In the SCIM, the stator core is magnetized by currents originating from the grid terminals. Conductive bars arranged on the rotor allow for currents to be generated in these bars as the stator magnetic field rotates through the stator core. Thus, the currents in the rotor bars induce a magnetic field in the rotor core. The interaction of rotor and stator flux gives rise to electromagnetic torque, thus accelerating the shaft. Replacing the conductive bars with copper windings, and providing access to the rotor winding terminals via a slip ring allows one to directly control the rotor current and flux, thereby controlling the amount of torque and grid-terminal reactive power.

Configuration of the doubly-fed induction machine is not limited to a grid-connected stator (herein referred to as the “stator-tied" configuration). In fact, the grid can be connected to the rotor terminals (herein referred to as the “rotor-tied" configuration), creating a magnetic field in the rotor core, which induces a current in the stator windings, and thus, a magnetic field in the stator core. Torque production is achieved in a similar manner, by controlling the interaction

of rotor and stator flux. In this configuration, the electronic power converter is used to regulate the stator magnetic field, to generate a specific amount of torque and remain synchronized with the magnetic field existing in the rotor core. Operation of the WECS in this proposed configuration is not well understood, and is studied here in more detail. Characterization of machine performance, compared to the conventional configuration, is particularly interesting.

Theory Of The Rotor-tied DFIG For Wind Energy Conversion

By moving the grid induced magnetic field to the rotor, magnetic losses can be minimized due to changes in the material's frequency of magnetization. Using some generalizations regarding machine core dimensions, we find that the rotor core is typically of smaller volume than the stator core. So shifting the higher grid frequency (60 Hz) to the rotor core, and the slower converter frequency ([-30,30] Hz) to the larger stator core, reduces the magnetic hysteresis loss. Furthermore, the extent to which the loss is reduced is directly related to the number of poles the machine has. Machines with a smaller number of poles reap larger benefits than those with a larger number of poles; DFIGs used in wind turbines usually have four or six poles.

Theoretical analysis of the efficiency improvements requires the per-phase equivalent circuit machine parameters, along with knowledge of the operating flux density in the core material, hysteresis loss parameters associated with the material, and an estimate of the rotor and store core dimensions. Several machines encountered in WECS literature are studied to determine if any benefits could exist by operating in the rotor-tied configuration. The equivalent circuit parameters of these machines are provided in [1], [5]–[6]. Assumptions of the core materials and flux densities are consistent through the machines, and are estimated based on typical materials used in the construction of electric machines [7]. Volume estimations are based on approximate machine dimensions.

For each of the machines considered, the theoretical analysis shows increased efficiency when operated in the proposed configuration. Using statistical methods [8], [9], the impact on annual energy production is approximated, with results showing a considerable increase. The analysis also shows that because the converter power handling capability is maintained between configurations, it is possible to use the same power electronic hardware to control the machine

in both configurations.

Control And Experimental Performance Of The Rotor-tied DFIG

Although hysteresis loss is a major component of core loss within the machine, there are additional types of magnetic and ohmic losses that contribute to the overall efficiency as well [3], [10]. Because it is impossible to accurately model every aspect of the system, only experimental comparison can provide the most accurate conclusions regarding any benefits of operating in the rotor-tied configuration.

In the experiments performed here, we constructed a back-to-back converter similar to those used in commercial wind turbines [1]. The machine under test is driven by a dynamometer, with the same rotational direction for both configurations. We control the machine using simple proportional plus integral (PI) controllers. The same type of controller, with similar control response, is used for both configurations. Operation in the rotor-tied configuration is experimentally validated, with voltages and currents that closely match theoretical values. By measuring the input power delivered to the shaft, and the output power at the machine terminals, we provide an experimental comparison of steady-state performance. The proposed configuration is found to be considerably more efficient. Statistical analyses show that this technology could have a significant impact on annual energy production.

Thesis Organization

The two following chapters are composed of work that has been published in or has been submitted to a conference publication.

Chapter 2 studies the theory of operating the DFIG in the rotor-tied configuration. Operating regions are explored with a desirable operating region identified. Steady-state conditions are characterized for both configurations, including estimated core losses and conversion efficiency. The redistribution of currents and losses is readily observed. Efficiency and annual energy figures are computed for each configuration, with results motivating experimental validation.

Chapter 3 covers control and operation of the DFIG in the rotor-tied configuration, and provides experimental comparison to the conventional stator-tied configuration. PI controllers

are developed to control the stator current, electromagnetic torque, and rotor reactive power for the rotor-tied configuration. Experiments are performed on a 7.5 kW DFIG. The machine is operated in similar manners for each configuration, with a dynamometer used to emulate the incoming wind power. Performance of the machine is characterized by physical measurements. Conclusions regarding performance in the proposed configuration are drawn, providing insight to the preferred configuration for wind energy conversion systems.

Chapter 4 concludes this work with a summery of results and a discussion of the implications that operating in the proposed configuration may have. Additional studies which must be performed before fully validating adoption of this technology are also discussed.

It is important to note that in Chapter 2, we refer to the frequency of magnetization in the stator core by the variable ω_s, and in Chapter 3, we refer to it by ω_e.

CHAPTER 2. DFIG WITH GRID-CONNECTED ROTOR FOR WIND ENERGY CONVERSION SYSTEM

A paper published in the *Proceedings of the IEEE International Electric Machines and Drives Conference*, 2013

Nicholas David[1] and Dionysios Aliprantis

2.1 Abstract

This paper explores an alternative connection of a wind turbine with doubly-fed induction generator to the power system, inverse to the conventional topology. In the proposed configuration, the rotor windings are directly connected to the grid, while the stator is connected through a power converter. This configuration could be preferable in terms of energy conversion efficiency, depending on the machine's circuit parameters and physical dimensions.

2.2 Introduction

Wind turbines with wound-rotor induction generators are very common. They are typically operated with the stator windings directly connected to the grid via a step-up transformer, and the rotor windings coupled through a power converter, which is rated at 30–40% of maximum turbine power output. This is called the Type-3 topology, or the doubly-fed induction generator (DFIG).

Here, we consider reversing the connections so that the rotor windings are connected directly to the grid, whereas the stator windings are interfaced through the power converter. This idea

[1] Primary researcher and author

was recently proposed by You et al. [11], where it was concluded that the physical size of the machine can be reduced when designed specifically for rotor-tied operation. This configuration is analyzed in the steady state, in the context of a variable-speed wind energy conversion system. It is found that the DFIG with grid-connected rotor yields substantial improvement in energy conversion efficiency.

The paper is structured as follows. In Section II, the machine operating modes are studied to determine the desired operating region. Core loss estimates are derived in Section III. In Section IV, eight machines are studied in both the rotor-tied and stator-tied configurations, in the context of wind energy conversion. Conclusions regarding the preferred configuration are provided in Section V.

2.3 Machine Operating Modes

Assume that the rotor of a wound-rotor induction generator is connected to a 60-Hz power system, as shown in Fig. 2.1. The stator is interfaced to the grid through a power electronic converter, which is composed of a stator-side converter (SSC), dc-link, and grid-side converter (GSC). Then, in the steady state, the frequency of stator electrical quantities, ω_s, and the rotor electrical speed, ω_r, are related by $\omega_s = \omega_r + 2\pi 60$, in rad/s. The classical definition of slip is still valid in this new configuration:

$$s = \frac{\omega_s - \omega_r}{\omega_s} = \frac{2\pi 60}{\omega_r + 2\pi 60}. \tag{2.1}$$

A plot of the slip vs. rotor electrical speed is shown in Fig. 2.2.

It is useful to consider the flow of power in the machine. Assume that the stator terminal power, P_s, rotor terminal power, P_r, and mechanical power, P_m, are all defined positive entering the machine. These powers are related by the following well-known equations:

$$P_s \approx -\frac{1}{1-s} P_m \tag{2.2}$$

$$P_r \approx -sP_s\,. \tag{2.3}$$

Three distinct operating regions can be identified, defined by: (i) $s \geq 1$, (ii) $0 < s < 1$, and (iii) $s < 0$. These are delineated by the green horizontal lines in Fig. 2.2.

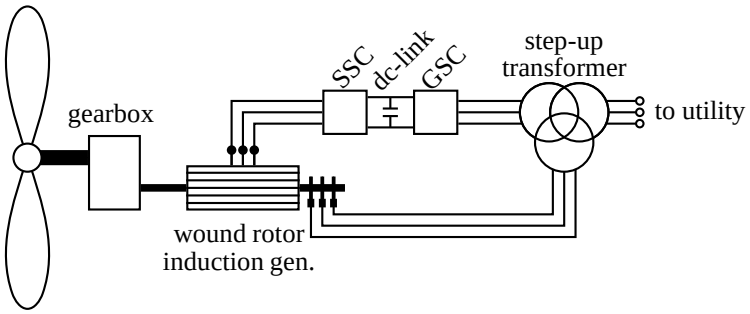

Figure 2.1 Topology of a Type-3 wind generator in the rotor-tied configuration. (Note: Not shown is an auxiliary crowbar circuit that is used to protect the power electronics during power system faults.)

The first region, where $s \geq 1$, corresponds to rotor electrical speed in the range $[-2\pi 60, 0]$ rad/s. In this region, the stator absorbs power and the rotor generates power. Here, $|P_r| > |P_s|$. As ω_r approaches $-2\pi 60$ rad/s, the slip approaches $+\infty$, so the stator terminal power approaches zero (the stator winding carries dc current when $\omega_r = -2\pi 60$ rad/s), and the rotor carries the entire mechanical power. This region can be interpreted as similar to the classical "subsynchronous" mode of the stator-tied DFIG.

The second region, where $0 < s < 1$, corresponds to positive rotor speed, $\omega_r > 0$. In this region, the rotor absorbs power and the stator generates power. Because $|P_s| > |P_r| > P_m$, operation in this region is not particularly attractive.

The third region, where $s < 0$, corresponds to rotor electrical speed in the range $(-\infty, -2\pi 60)$ rad/s. In this region, both stator and rotor generate power. As ω_r approaches $-2\pi 60$ rad/s, the slip approaches $-\infty$. As $\omega_r \to -\infty$, the rotor terminal power is reduced and the stator terminal power approaches the mechanical power. This region is similar to the classical "supersynchronous" mode of the stator-tied DFIG. Operation in the first and third regions (where the electrical rotor speed is negative) is the preferred mode of operation, and studied further in the next section.

Imposing an upper limit on the stator converter power helps identify the operating region of the rotor-tied DFIG. Typically, the power electronic converter in DFIGs is rated to 1/3 of the maximum mechanical power, which increases quasi-cubically with rotor speed in a variable-speed wind turbine. Therefore, using (2.2) and (2.3), it can be seen that the most negative slip

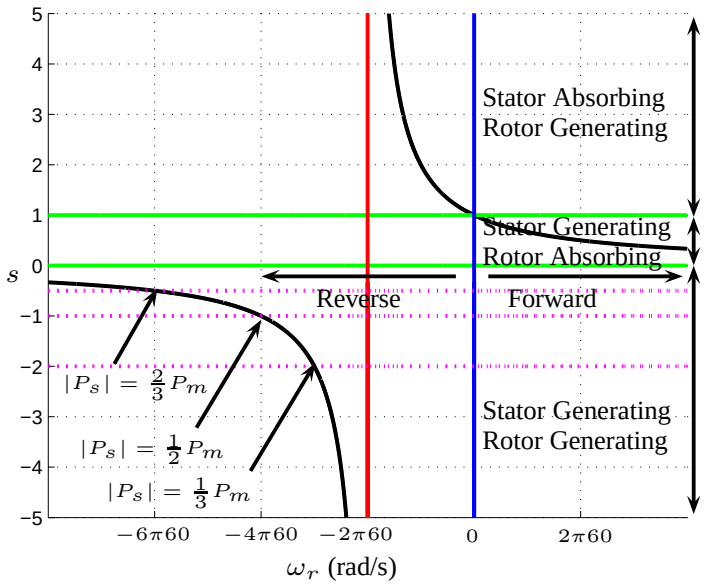

Figure 2.2 Operating regions for the proposed configuration (for a 60-Hz system).

cannot exceed $s = -2$ (the "fastest" rotor speed is $\omega_r = -3\pi 60$ rad/s), and the most positive slip is $s = 2$ (the "slowest" rotor speed is $\omega_r = -\pi 60$ rad/s). Hence, the rotor-tied DFIG shall operate within the region $-3\pi 60 \leq \omega_r \leq -\pi 60$ rad/s, turning in "reverse," that is, in the opposite direction from the rotating magnetomotive force (mmf) created by the rotor currents. At low wind speeds, the stator mmf rotates in the positive direction, but as the wind speed increases and the rotor accelerates in the negative direction, the stator mmf slows down, and eventually reverses its direction of rotation. The power electronic converter controls the stator current waveforms to achieve this behavior.

The classical steady-state T-equivalent circuit of the induction machine is still valid in the rotor-tied configuration. Now, the rotor voltage and frequency have fixed (grid-imposed) values. Ignoring the voltage drops across the winding resistances and leakage reactances, the rotor and stator terminal voltage phasors are approximately related by $\tilde{V}_s \approx \tilde{V}_r'/s$, where prime denotes referral to stator. Therefore, in the speed range $-3\pi 60 \leq \omega_r \leq -\pi 60$ rad/s, where $|s| > 2$, the stator voltage will be less than the (referred) rotor voltage. This is similar to what happens in the conventional configuration, where the (referred) rotor voltage is less than the stator voltage. In the ensuing analysis, we apply the same (referred) voltage magnitude to the rotor terminals as would be applied to the stator terminals in the conventional configuration.

As will be shown, the topology change from stator- to rotor-tied impacts the current levels in the machine for any given operating point (i.e., for a given wind speed and electromagnetic torque level). This in turn impacts the respective ohmic losses incurred during operation, which can be estimated in a straightforward manner using the T-equivalent circuit. However, the core loss component is also important, as discussed next.

2.4 Core Loss Estimation

We estimate the core loss in a generic wound-rotor induction machine, based on the cross-section of Fig. 2.3 and the following simplifying assumptions. Four distinct regions labeled A–D can be identified in the ferromagnetic material. Region A is the stator yoke extending to a radius r_o, B is the region of the stator teeth, C is the region of the rotor teeth, and region D is the rotor yoke. The air-gap is at radius r_a and is considered to have negligible thickness. It is assumed that the machine is dimensioned so that it carries the same maximum flux density throughout its magnetic material. The stator slots are assumed to penetrate to the middle of the stator, having a height of $(r_o - r_a)/2$. The rotor slots have the same height as the stator slots.

Assuming that the windings are (approximately) sinusoidally distributed, the variation with time of the fundamental component of the air-gap flux density at angular position ϕ_s can be expressed as

$$B\left(\phi_s, t\right) = B_g \sin\left(\omega_s t + \frac{P}{2}\phi_s\right) \tag{2.4}$$

where B_g is the peak value. Hence, the total flux per pole can be calculated by

$$\Phi_{\text{pole}} = l r_a \int_0^{\frac{2\pi}{P}} B_g \sin\left(\frac{P}{2}\phi_s\right) d\phi_s = \frac{4}{P} l r_a B_g \tag{2.5}$$

where l is the stack length.

In region A, the maximum flux through the cross-sectional area of the yoke occurs in the middle between a north and south pole, and can be approximated by

$$\Phi_A = \frac{\Phi_{\text{pole}}}{2} = \frac{2}{P} l r_a B_g = B_A l \left(\frac{r_o - r_a}{2}\right) \tag{2.6}$$

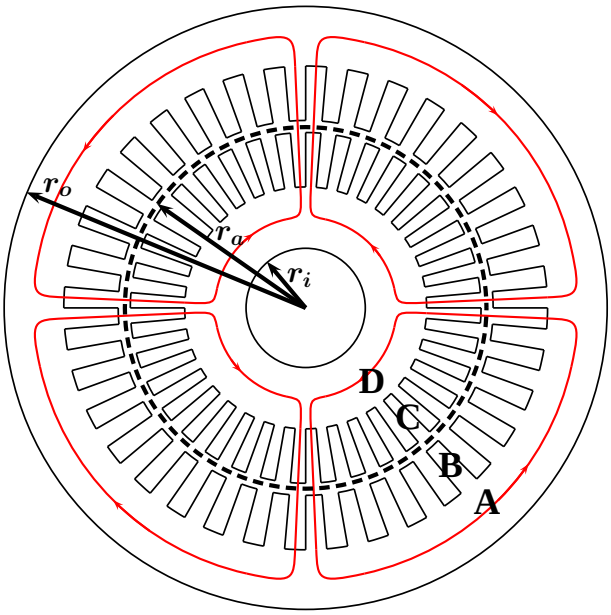

Figure 2.3 Generic cross-section of a wound-rotor induction machine (shown here with 4-poles), and magnetizing flux path.

assuming constant flux density B_A at that angular position in region A. Similarly, we can express the maximum flux through the rotor yoke (region D) by

$$\Phi_D = \frac{\Phi_{\text{pole}}}{2} = B_D l \left(r_a - \frac{r_o - r_a}{2} - r_i \right). \tag{2.7}$$

We assume that the teeth and slot areas are equally divided, so the maximum flux density in the stator and rotor teeth (directly across from north and south poles in regions B and C) is

$$B_B = B_C = 2B_{\text{g}}\,. \tag{2.8}$$

Using (2.6) and (2.8) and the fact that $B_A = B_B$ leads to the following relationship between the outer radius of the stator core, the air-gap radius, and the number of poles:

$$r_o = \left(1 + \frac{2}{P}\right) r_a\,. \tag{2.9}$$

Equating (2.6) and (2.7), and using (2.9) and $B_A = B_D$, yields the following relationship between the inner radius of the rotor yoke (which defines an approximate boundary for the magnetic flux), the air-gap radius, and the number of poles:

$$r_i = 2r_a - r_o = \left(1 - \frac{2}{P}\right) r_a\,. \tag{2.10}$$

Table 2.1 Core Volume Comparison for P-Pole Machines

	Number of Poles, P				
	2	4	6	8	16
$\frac{\text{Vol}_s}{\text{Vol}_r} = \frac{3P+7/2}{3P-7/2}$	3.8	1.82	1.48	1.34	1.15

These general equations allow one to calculate the volume of the stator and rotor regions, which after algebraic manipulations are expressed as follows:

$$\text{Vol}_A = \left[\pi r_o^2 - \pi\left(\frac{r_o + r_a}{2}\right)^2\right] l = \frac{\pi l r_a^2}{P^2}\left(2P + 3\right) \tag{2.11}$$

$$\text{Vol}_B = \frac{1}{2}\left[\pi\left(\frac{r_o + r_a}{2}\right)^2 - \pi r_a^2\right] l = \frac{\pi l r_a^2}{P^2}\left(P + \frac{1}{2}\right) \tag{2.12}$$

$$\text{Vol}_s = \text{Vol}_A + \text{Vol}_B = \frac{\pi l r_a^2}{P^2}\left(3P + \frac{7}{2}\right) \tag{2.13}$$

$$\text{Vol}_C = \frac{1}{2}\left[\pi r_a^2 - \pi\left(\frac{3r_a - r_o}{2}\right)^2\right] l = \frac{\pi l r_a^2}{P^2}\left(P - \frac{1}{2}\right) \tag{2.14}$$

$$\text{Vol}_D = \left[\pi\left(\frac{3r_a - r_o}{2}\right)^2 - \pi r_i^2\right] l = \frac{\pi l r_a^2}{P^2}\left(2P - 3\right) \tag{2.15}$$

$$\text{Vol}_r = \text{Vol}_C + \text{Vol}_D = \frac{\pi l r_a^2}{P^2}\left(3P - \frac{7}{2}\right). \tag{2.16}$$

The ratio of the stator and rotor volumes is

$$\frac{\text{Vol}_s}{\text{Vol}_r} = \frac{3P + \frac{7}{2}}{3P - \frac{7}{2}} \tag{2.17}$$

which is always larger than one, but as the number of poles is increased the volumes tend to become equal to each other. A comparison of the stator to rotor volume ratios for various number of poles is provided in Table 2.1.

The core loss is assumed to be dominated by the hysteresis loss, which for each region $x = \{A, B, C, D\}$ is [10], [12]

$$P_{c,x} = \left(k_h B_{\text{max},x}^n f_x\right)\left(\text{Vol}_x\right)\left(\rho\right) \tag{2.18}$$

where ρ is the density of the core material, f_x is the frequency of magnetization, $B_{\text{max},x}$ is the maximum flux density, n is the hysteresis exponent, k_h is the hysteresis coefficient, and Vol_x is the volume of core material. The total core loss is the sum of the loss from each region, and will vary with operating point due to the change in stator frequency.

In the ensuing analysis, we assume the core material is DI-MAX M-15-FP steel [7]. Typical core loss information provided by the manufacturer suggests a hysteresis coefficient of $k_h = 0.0150$ J/ (kg · cycle · T^n). The hysteresis exponent is not provided, so we assume a value of $n = 2$. This material has density $\rho \approx 7650$ kg/m^3. It is assumed that the machine has the same maximum flux density throughout all regions, with $B_{\max,x} = 1.5$ T, and that this value does not change with operating point.

Because the grid-tied side of the machine will always have a magnetization frequency of 60 Hz, it is clear that connecting the smaller-volume side of the machine to the grid will minimize the total core loss. In the rotor-tied configuration, the rotor is magnetized with the grid frequency, i.e., $f_C = f_D = 60$ Hz, and the stator is magnetized with variable frequency, $f_A = f_B = 60/s$ Hz. While operating in the region described in section II, the stator frequency will vary in the range $[-30, 30]$ Hz.

2.5 Case Studies

Eight machines with equivalent-circuit parameters obtained from [1] and [5]–[6] are studied to determine their preferred configuration (rotor-tied or stator-tied). Their characteristics are summarized in Table 2.2, where primed circuit parameters are referred to the stator. Note that several machines are rated for 50 Hz, and as such, are simulated for a grid frequency of 50 Hz rather than 60 Hz. Lacking adequate information regarding the design details of each machine, and for the sake of comparison, the air-gap radius, r_a, and stack length, l, are assumed values.

Variable-speed horizontal-axis wind turbines are considered, controlled for maximum power extraction

$$P(v_w) = \frac{1}{2}\rho C_p A v_w^3 , \tag{2.19}$$

where $\rho = 1.25$ kg/m^3 is the density of the air, $C_p = 0.45$ is the performance coefficient (assumed constant for simplicity), A is the swept area of the blades, and v_w is the incoming upstream wind speed. For each turbine, the cut-in wind speed is 4 m/s, and the rated wind speed is near 12 m/s. To this end, the swept area and gear ratio are chosen such that the wind speed range $[4, 12]$ m/s corresponds closely to the variable electrical frequency range $[-30, 30]$ Hz, with the

Table 2.2 Summary of Machine Characteristics

Machine	1 [13]	2[6]	3 [14], [15]	4 [1]	5 [5]	6 [5]	7 [5]	8 [5]
P_{rated} (kW)	1700	1500	2000	2000	1500	1000	5000	6000
V_{rated} (V)	690	575	690	690	690	575	950	4000
f_{rated} (Hz)	50	60	50	50	50	60	50	50
P	4	6	4	4	4	4	6	6
R_s (mΩ)	1.615	1.565	2.199	1.164	2.650	3.654	1.552	26.86
L_{ls} (mH)	0.09177	0.1002	0.12003	0.07003	0.1687	0.1304	1.2721	0.23142
R'_r (mΩ)	2.369	1.102	1.799	1.310	2.630	3.569	1.446	25.74
L'_{lr} (mH)	0.08203	0.0914	0.0500	0.0754	0.1337	0.1198	1.1194	0.2183
L_m (mH)	2.5076	1.696	2.9000	2.995	5.4749	4.12	5.5182	25.908
r_a (m)	0.55	0.50	0.60	0.60	0.50	0.35	0.8	0.9
l (m)	1.55	1.50	1.60	1.60	1.50	1.35	2.0	2.1
Vol_s (m^3)	1.4270	0.7036	1.753	1.753	1.1413	0.5033	2.4016	3.1915
Vol_r (m^3)	0.7825	0.4745	0.9613	0.9613	0.6259	0.2760	1.6197	2.1524

"infinite slip" speed near 8 m/s. For a 50-Hz power system, the variable frequency range is $[-25, 25]$ Hz.

Each machine was studied in both the rotor-tied and stator-tied configurations. The standard steady-state per-phase T-equivalent circuit is solved over the range of operating wind speeds, under the assumption that the grid-tied terminal operates at unity power factor (set by the power electronic converter that controls the currents flowing in the other side). The shaft power, P_m, rotor terminal power, P_r, and stator terminal power, P_s, are defined positive entering the machine. Resistive losses, P_{R_s} and $P_{R'_r}$, and core loss, P_c, are defined positive exiting the machine. The equivalent circuit is solved using an iterative method to satisfy a power balance equation:

$$P_m + P_r + P_s - P_{R_s} - P_{R'_r} - P_c = 0. \tag{2.20}$$

The stator and rotor frequencies, terminal voltages, line currents, and terminal powers are shown for machine 1 in Fig. 2.4. In the rotor-tied configuration, these quantities vary in a similar, but opposite, fashion as in the stator-tied configuration. In the rotor-tied configuration, the rotor current tends to be reduced whereas the stator current tends to be increased. This would be advantageous in a machine with higher rotor than stator resistance ($R'_r > R_s$), because I^2R losses would be reduced overall.

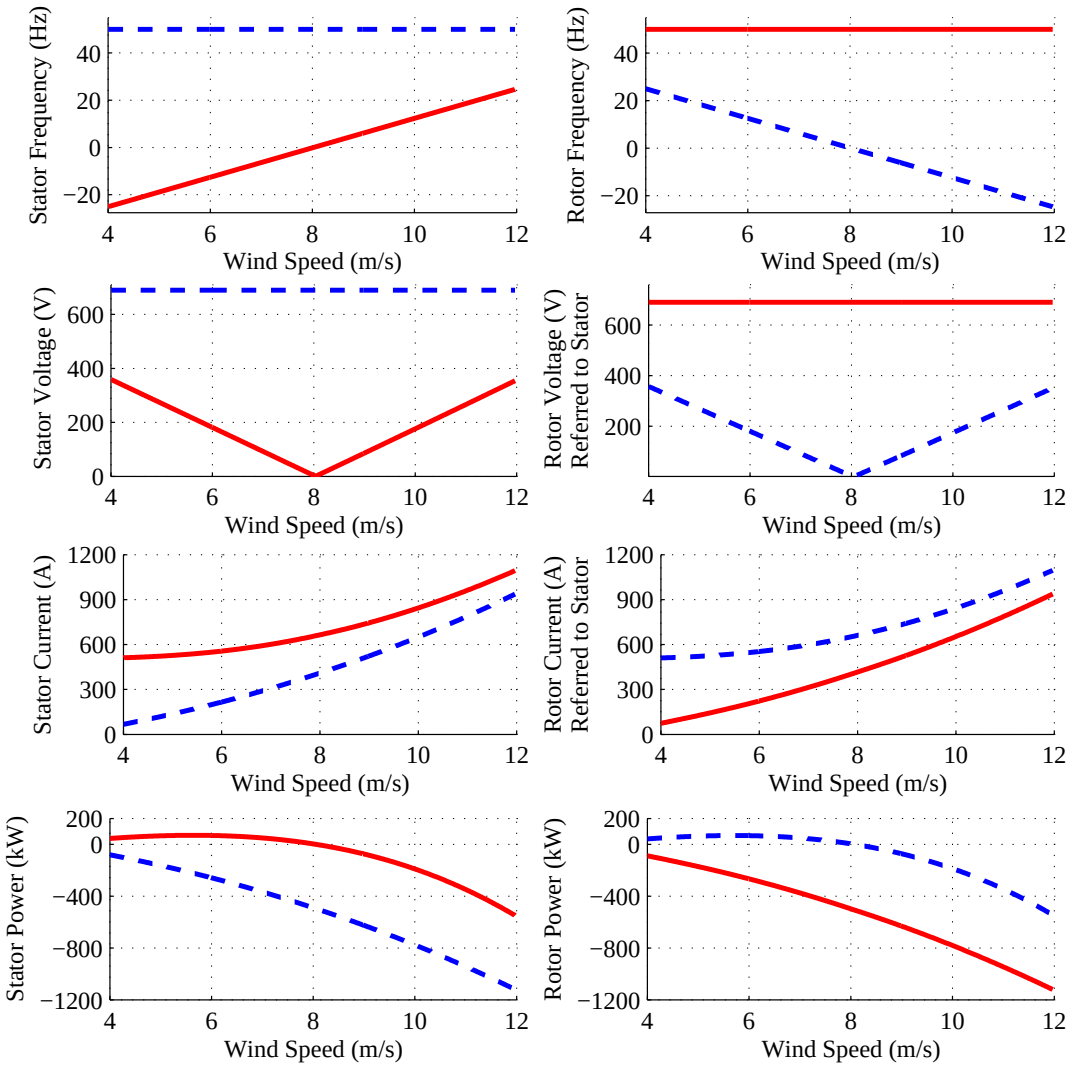

Figure 2.4 Frequencies, terminal voltages, line currents, and powers over the operating wind speed range for machine 1. (Rotor-tied: solid, stator-tied: dashed.)

It can also be observed that applying the lower, variable frequency to the stator (which has larger volume than the rotor) will reduce the total core loss. As a result, the efficiency of the machine can be increased by operating in the rotor-tied configuration. The ohmic losses, core losses, and resulting efficiencies are shown for machine 1 in Fig. 2.5. As a result of connecting the rotor to the grid, under the assumptions previously posed, the conversion efficiency is increased over the entire wind speed range. The results for machines 2–8 follow similar trends.

Operating the DFIG in the rotor-tied configuration results in improved operating efficiency. The annual energy savings can be calculated by considering wind speed statistics. The Weibull

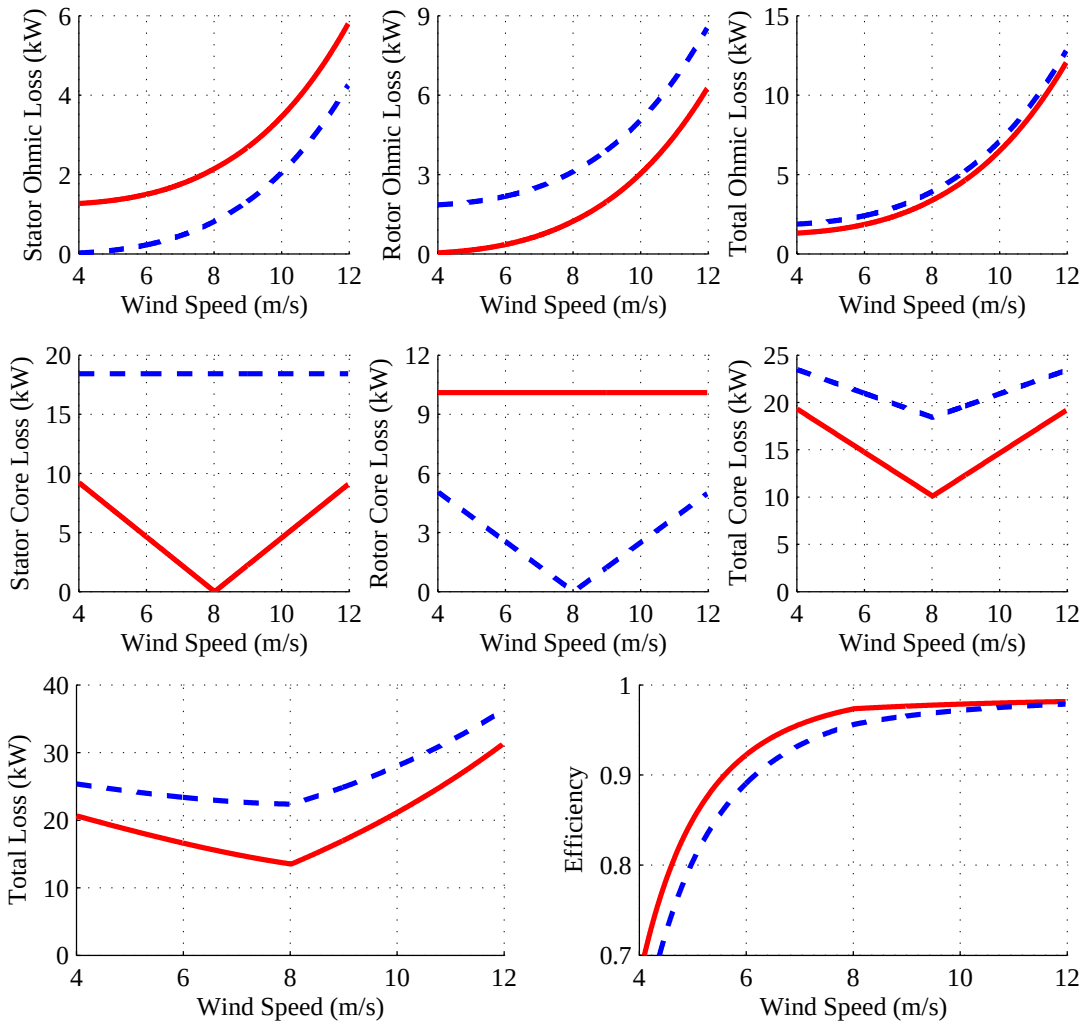

Figure 2.5 Ohmic loss, core loss, total loss, and resulting efficiency for machine 1. (Rotor-tied: solid, stator-tied: dashed.)

probability density function is used to describe the annual variation of wind speed [8]

$$f\left(v_w\right) = \frac{k}{c}\left(\frac{v_w}{c}\right)^{k-1} e^{-(v_w/c)^k} \tag{2.21}$$

where c is the scale factor, k is the shape factor, and v_w is the wind speed. Here, we assume values of $k = 2$ and $c = 8.3$ m/s; the resulting average wind speed is $\bar{v}_w = 7.4$ m/s.

Annual energy generation is computed by

$$E_{\text{gen}} = 8760 \int_{v_w^{\text{in}}}^{v_w^{\text{out}}} P_{\text{gen}}(v_w) f(v_w) dv_w \tag{2.22}$$

where $P_{\text{gen}}(v_w) = -[P_r(v_w) + P_s(v_w)]$. The cut-in wind speed is taken to be $v_w^{\text{in}} = 4$ m/s, and the cut-out wind speed is taken to be $v_w^{\text{out}} = 25$ m/s. For wind speeds beyond rated

Table 2.3 Annual Energy Summary

Machine	1	2	3	4	5	6	7	8
Generated (Rotor-Tied)	4800.3	4681.8	5574.4	5692.0	4253.7	2806.7	14240.0	17028.7
Generated (Stator-Tied)	4754.4	4667.2	5524.7	5640.6	4220.5	2789.3	14189.0	16964.1
Lost (Rotor-Tied)	140.82 (2.85%)	104.50 (2.18%)	174.48 (3.04%)	157.11 (2.69%)	115.03 (2.63%)	72.381 (2.51%)	317.16 (2.18%)	446.40 (2.55%)
Lost (Stator-Tied)	186.74 (3.78%)	119.13 (2.49%)	224.17 (3.90%)	208.55 (3.57%)	148.24 (3.39%)	89.817 (3.12%)	368.14 (2.53%)	510.95 (2.93%)

value, approximately 12 m/s, the machine operates at rated power. Under the assumed wind resource, the annual energy generated and lost while operating in both the rotor- and stator-tied configurations is listed for each machine in Table 2.3. Clearly, operating in the rotor-tied configuration can result in significant energy savings.

2.6 Conclusion

In this paper, we analyzed a set of 8 DFIGs in a series of steady-state operating conditions, corresponding to the entire wind speed range that is typically encountered in variable-speed wind energy conversion systems. Under certain reasonable assumptions regarding the dimensions of the core structures, we concluded that operating these DFIGs in the rotor-tied configuration can result in significant energy savings, on the order of 0.5–1%. Increased efficiency results from energizing the higher-volume side (stator) with the lower frequency, thereby reducing hysteresis loss. Eddy current loss was not considered here, but is expected to follow a similar trend, thus further improving efficiency. With regards to the power electronics, a partially rated converter will be needed, as in the stator-tied case, with the same functionality as before; so the machine drive is not expected to be a cause of concern. In fact, it might prove possible to retrofit existing DFIGs for operation in the proposed rotor-tied configuration using equipment already in place. Therefore, our results indicate that the rotor-tied configuration could be an interesting alternative to the more typical stator-tied configuration. Nevertheless, further studies that take into account electrical, mechanical, and thermal design details, including reinforcing the slip-ring/brush configuration for carrying a larger amount of power, are necessary to establish the benefits of the rotor-tied generator.

CHAPTER 3. IMPROVED EFFICIENCY OF DFIG WIND ENERGY CONVERSION SYSTEMS BY OPERATING IN THE ROTOR-TIED CONFIGURATION

A paper submitted to the *International Conference on Electrical Machines*, 2014

Nicholas David[1] and Dionysios Aliprantis

3.1 Abstract

An alternative connection topology for a wind turbine with doubly-fed induction generator is explored, with the rotor tied directly to the power grid and the stator connected through a power electronic converter. Control algorithms are developed for the new configuration. Experiments are performed on a 7.5-kW machine to evaluate the proposed topology. The proposed configuration is found to be more efficient than current practice.

3.2 Introduction

Wind turbines with wound-rotor induction generators are very common. They are typically operated with the stator windings directly connected to the grid via a step-up transformer, and the rotor windings coupled through a power converter, which is rated at 30–40% of maximum turbine power output. This is called the Type-3 topology, or the doubly-fed induction generator (DFIG).

As a means to improve the energy conversion efficiency of the machine, we consider reversing the connections so that the rotor windings are connected directly to the grid, whereas

[1] Primary researcher and author

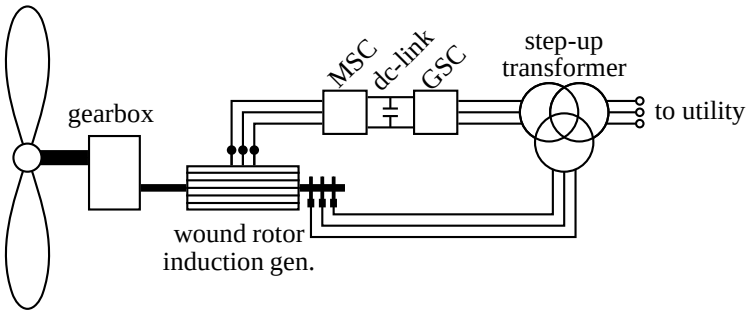

Figure 3.1 Topology of a Type-3 wind generator in the rotor-tied configuration. (Note: Not shown is an auxiliary crowbar circuit that is used to protect the power electronics during power system faults.)

the stator windings are interfaced through the power converter consisting of a machine-side converter (MSC), dc-link, and a grid-side converter (GSC), as depicted in Fig. 3.1. The proposed configuration is herein referred to as "rotor-tied," and the conventional configuration as "stator-tied."

This idea was recently proposed by You et al. [11], where it was concluded that the physical size of the machine can be reduced when designed specifically for rotor-tied operation. Steady-state operation of such a DFIG was studied in the context of a variable-speed wind energy conversion system in [16]. Therein, an appropriate operating region (slip and rotor speed) was determined based on the electronic power converter maximum power rating. Additionally, a variety of multi-MW machines were studied; for all of these, it was found that the rotor-tied DFIG could yield substantial improvement in energy conversion efficiency due to a reduction of magnetic hysteresis loss in the core of the machine. The total core loss is reduced due to the higher grid frequency (60 Hz) being moved to the smaller volume rotor core, and the lower converter frequency (approx. $[-30, 30]$ Hz) being moved to the larger volume stator core.

In this paper, we expand on that work by testing a 7.5-kW wound-rotor induction machine in both rotor-tied and stator-tied configurations. The machine parameters are listed in Appendix A. Experiments are performed at operating conditions that would typically be encountered in a variable-speed wind turbine.

3.3 Theoretical Considerations

To characterize the performance in the context of a wind energy conversion system, the machine under test is assumed to be representative of a DFIG wind turbine with a radius of swept area $r = 2.25$ m, gear ratio $g = 4.4$, and a constant tip-speed ratio of $\lambda = 8$. For these wind turbine parameters, the wind speed range of $v_{\mathrm{w}} = [4, 12]$ m/s corresponds to the slip range of $|s| > 2$ and $\omega_r = [-3\pi 60, -\pi 60]$ rad/s when in the rotor-tied configuration; this slip region results in the stator power converter handling up to one third of the maximum power output [16].

The torque applied to the (high-speed) generator shaft by the incoming wind stream, in terms of electrical rotor speed ω_r, is

$$T_L = \mathrm{sgn}\left(\omega_r\right) 0.5\rho\, C_p\, A \left(\frac{r}{g\lambda}\right)^3 \left(\frac{2}{P}\omega_r\right)^2. \tag{3.1}$$

where C_p is the performance coefficient, $A = \pi r^2$ is the blades' swept area, ρ is the air density, and P is the number of poles. In the stator-tied configuration, $T_L > 0$. In the rotor-tied configuration, $T_L < 0$, because the rotor is defined to rotate in the negative direction, and positive power is defined into the shaft. For operating in the rotor-tied configuration with $\rho = 1.25$ kg/m^3, $C_p = 0.45$, and $P = 6$, the torque applied to the shaft by the incoming wind stream is plotted in Fig. 3.2.

The friction and windage loss does not vary with configuration. To characterize the friction and windage loss for the machine in question, the shaft was driven with a dynamometer while both the stator and rotor were open-circuited. The speed of the shaft and the applied torque were measured, and the power required to overcome friction and windage was calculated; a polynomial curve was fit to the data. This data is useful in predicting the steady-state performance of the machine in the subsequent section.

Core loss is estimated by considering hysteresis alone [12], [16]

$$P_{c,x} = \left(k_h B_{\mathrm{max},x}^n f_x\right) \left(\mathrm{Vol}_x\right) \left(\gamma\right) \tag{3.2}$$

where γ is the material density, f_x is the frequency of magnetization, $B_{\mathrm{max},x}$ is the maximum flux density, and Vol_x is the volume of core material in region x of the machine. Lacking accurate

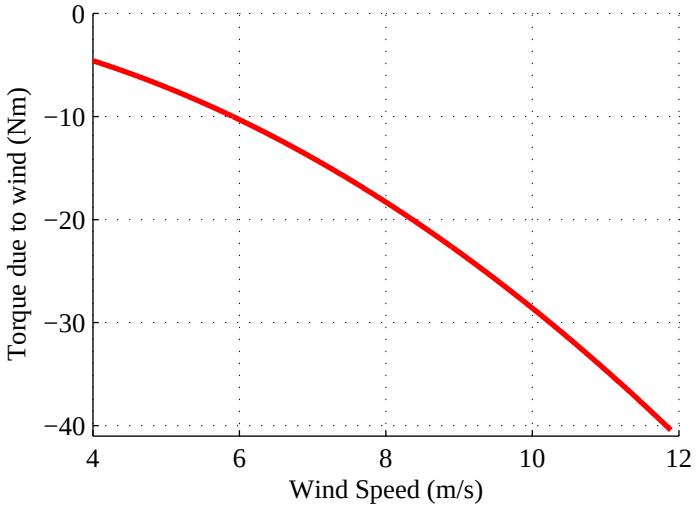

Figure 3.2 Torque applied to the shaft by the (virtual) incoming wind stream, when operating in the rotor-tied configuration.

knowledge of the core materials and physical dimensions, it is very difficult to accurately predict the maximum flux densities and core volumes. Additionaly, it has been found that the core loss variables k_h and n change with frequency [10]. Furthermore, harmonics caused by power converter switching and machine slots also add to the total core loss.

Without disassembling the machine to measure the rotor and stator core dimensions, we estimate the rotor and stator core volumes using the method detailed in[16]. From rough measurements of the length and radius of the machine, we estimate the stator and rotor core volumes to be $\text{Vol}_s = 1.47 \times 10^{-3}$ m^3 and $\text{Vol}_r = 9.95 \times 10^{-4}$ m^3. We also assume a constant maximum flux density in all regions of the machine, $B_{\max} = 1.3$ T, and a material density of $\gamma = 7650$ kg/m^3. The core loss parameters are also assumed constant, with $k_h = 0.015$ and $n = 12$ [7].

With the expected shaft torque, measurements of the friction and windage loss, and an estimate of the core losses, the theoretical per-phase equivalent circuit can be solved; these results are shown in Fig. 3.5. The corresponding losses, generation, and efficiency are shown in Fig. 3.6 and Fig. 3.7. In these figures, the red line corresponds to the rotor-tied configuration, and the blue line corresponds to the stator-tied configuration. This theoretical analysis only

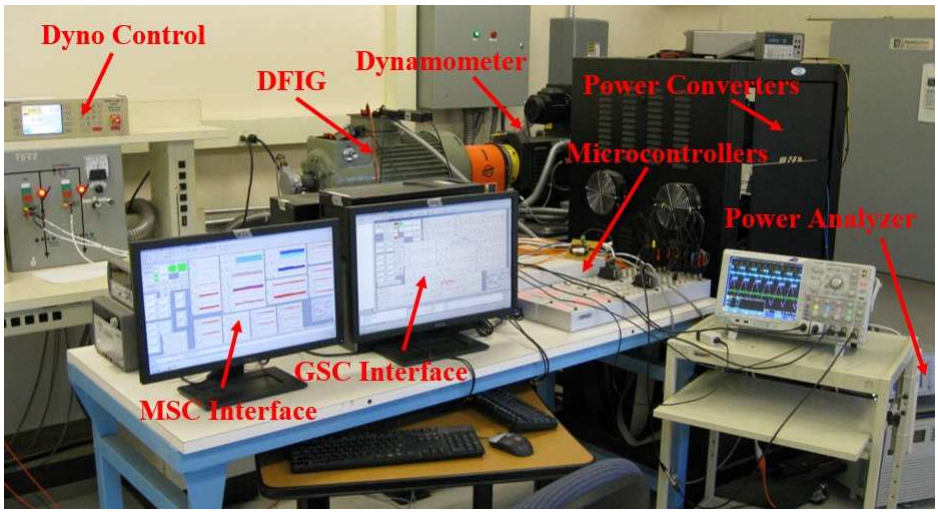

Figure 3.3 Experimental test stand for operating the DFIG in both rotor-tied and stator-tied configurations.

considers the fundamental components; machine slot and power switching harmonics are not considered. Due to the shift of grid-side and converter-side currents, ohmic losses are increased in the rotor-tied configuration. However, due to the shift of frequencies in the core material, the core loss is reduced by a greater amount. It is expected that the machine will be more efficient in the rotor-tied configuration.

3.4 Experimental Comparison

Experiment setup

To determine the preferred configuration (rotor-tied or stator-tied), the machine is operated at the same dynamometer torque, rotor speed, and grid-side reactive power for each configuration. The electromagnetic torque command is adjusted at the MSC interface until the torque displayed on the dynamometer controller matches that of (3.1). The same power electronic components are used interchangeably. A photo of the test stand is shown in Fig. 3.3.

These experiments focus on the performance of the DFIG itself, not the power converters and other auxiliary hardware (e.g., external reactors). The dynamometer input power includes that required to overcome friction and windage. Output power is measured at the machine

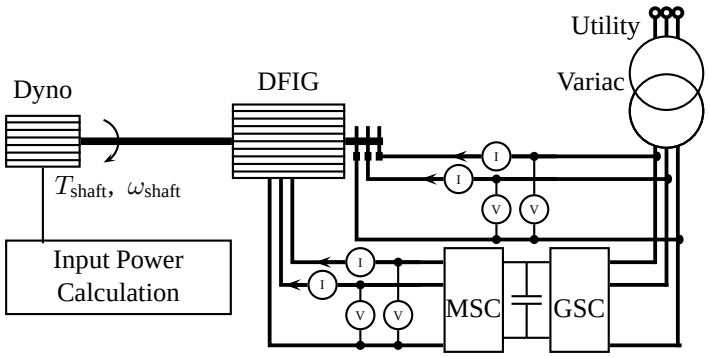

Figure 3.4 Test configuration for capturing input and output power while testing the DFIG. Not shown is a filter reactor between the GSC and Variac. (Rotor-tied configuration.)

terminals. Losses associated with the power converters and grid reactor are not considered. The average input and output power were measured simultaneously. A diagram showing the configuration of measurement equipment is provided in Fig. 3.4. Additional details regarding the experimental test stand are provided in Appendices C and D.

Results

The rotor and stator frequencies, fundamental voltages, fundamental currents, and fundamental terminal powers are plotted over the theoretical results in Fig. 3.5. Ohmic and core losses are shown in Fig. 3.6. These are calculated from the measured fundamental and total (harmonics included) line currents with the measured stator and rotor resistances. The core loss was obtained by subtracting the output, ohmic, and friction and windage losses from the input shaft power. The electromagnetic loss is the sum of ohmic and core loss; it is shown for all harmonics included. Because it is not possible to seperate the fundamental and harmonic core losses in the measured data, only the total core loss can be shown; this loss includes core loss due to switching and slot harmonics, as well as eddy current and other stray magnetic losses.

These results show that the resistive and core losses are shifted as predicted; the fundamental resistive losses are increased by approximately 50-100 W, but the core loss is reduced by approximately 200-300 W. The total core loss is very sensitive to the measured friction and windage

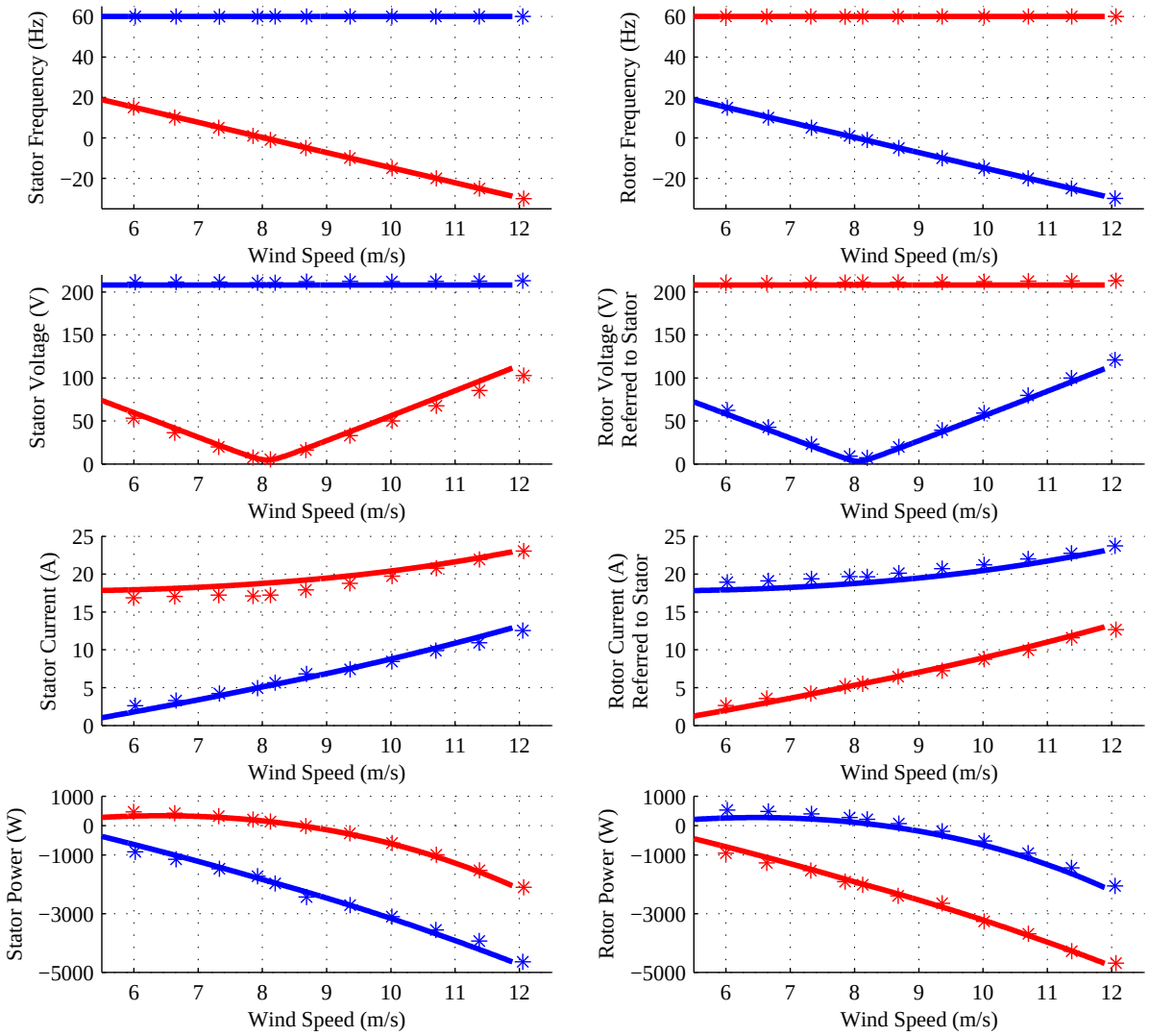

Figure 3.5 Comparison of theoretical and experimental results; shown are fundamental components only. (Rotor-tied: red, stator-tied: blue.)

loss, which is difficult to obtain consistently and accurately. The overall electromagnetic loss is reduced by about 200 W when operated in the rotor-tied configuration.

A significant discrepancy exists between the theoretical and measured core loss. In an ideal situation, the measured core loss should be larger than the theoretical, since the theoretical analysis did not consider eddy current loss or harmonic loss. However, the estimated core loss of (3.2) is very sensitive to the values of $B_{\max}$ and n, and cannot be tuned to fit the data any better. A more precise model of core loss should be used, one that provides for variability of parameter n with changes of frequency [10]. Another reason for the discrepancy could be

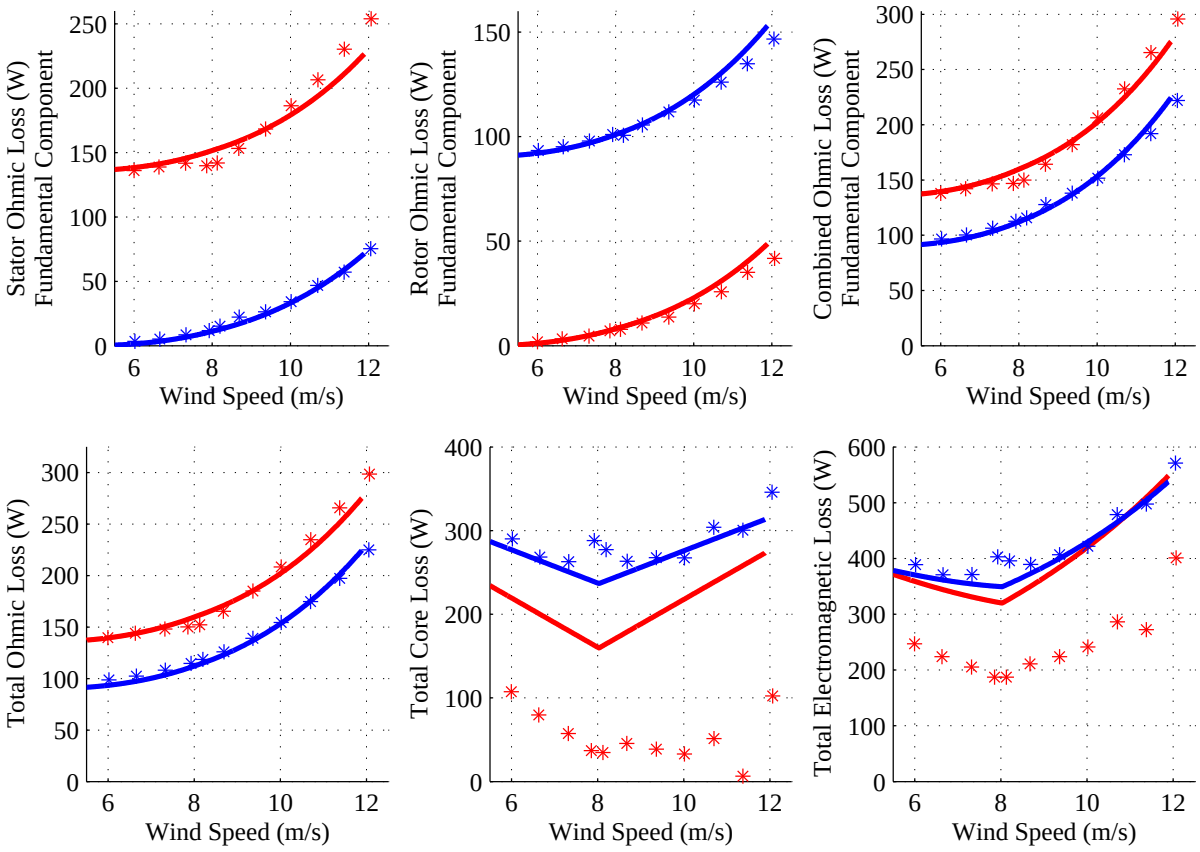

Figure 3.6 Electric and magnetic losses in the machine. (Rotor-tied: red, stator-tied: blue.)

error in the estimated volume of the rotor and stator cores and/or the maximum flux density throughout the machine.

Based on the experimental results, the rotor-tied configuration clearly leads to reduced core losses. The total loss, including ohmic, core, and friction and windage, and the overall energy conversion efficiency are shown in Fig. 3.7. Also shown is the total generation and efficiency based on fundamental output power. The rotor-tied configuration is 9.2% more efficient at synchronous speed than the stator-tied configuration, and 2.2% more efficient at rated power.

An interesting result comes from analyzing the voltage and current total harmonic distortion (THD), shown in Fig. 3.8. The converter voltage, stator current, and rotor current all have less THD in the rotor-tied configuration; it is reduced by 2–3%. This could be because the converter-side (real, non-referred) fundamental voltage is larger in the rotor-tied configuration, and the

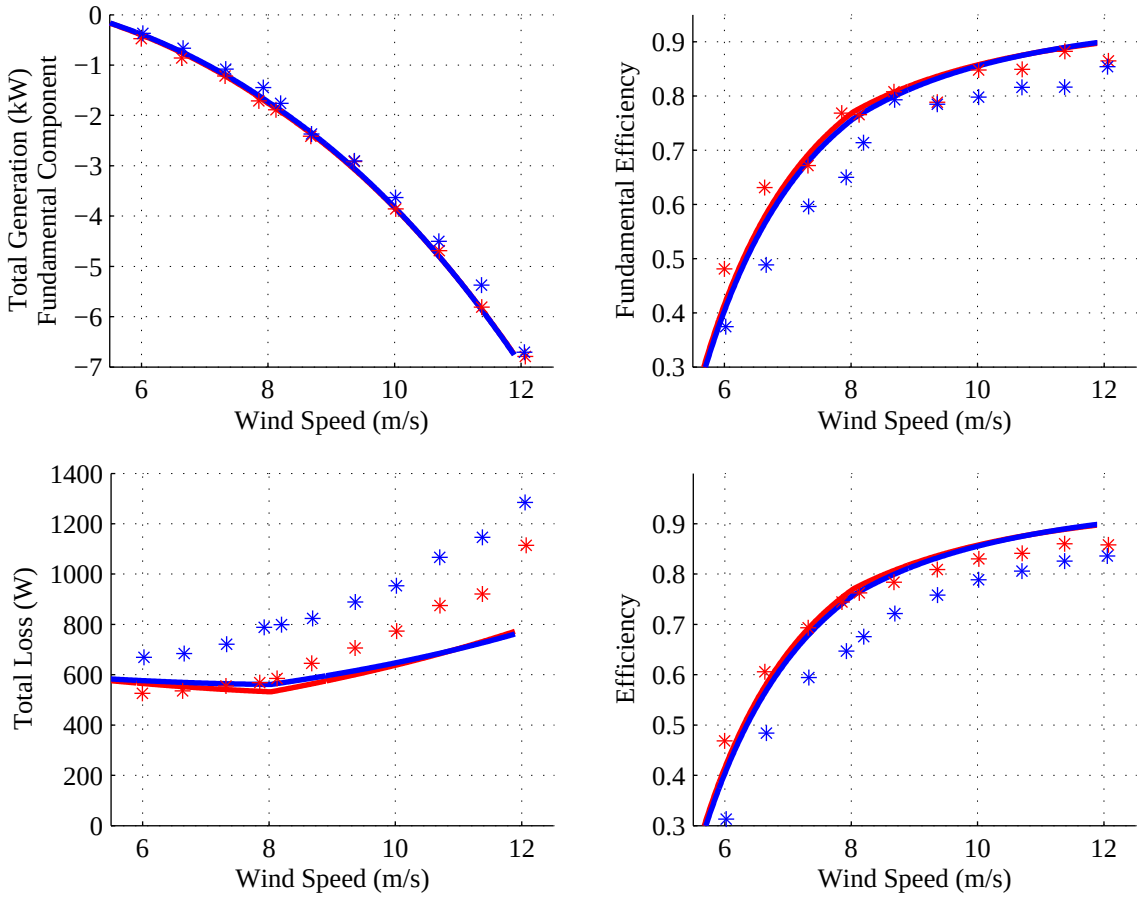

Figure 3.7 Total loss, generation, and efficiency. (Rotor-tied: red, stator-tied: blue.)

dc-link voltage used by the GSC is smaller; see Appendix C for details. Together, the larger voltage command and the smaller dc-link voltage result in a modulation index closer to 1, thus reducing the harmonic content due to space vector modulation (SVM).

At the 10 m/s operating speed, which corresponds to a shaft speed of 1500 rpm and dynamometer shaft torque of 28 Nm, the amount of rotor current THD in the rotor-tied configuration is 12%. For the same operating condition, the amount of stator current THD in the stator-tied configuration is 16%. While a filter reactor between the MSC and the machine terminals was not included here, these results suggest that for the rotor-tied configuration, a smaller filter reactor could be used to reduce the current harmonics than for the stator-tied configuration. This could possibly lead to reduced core losses in the filter reactor as well.

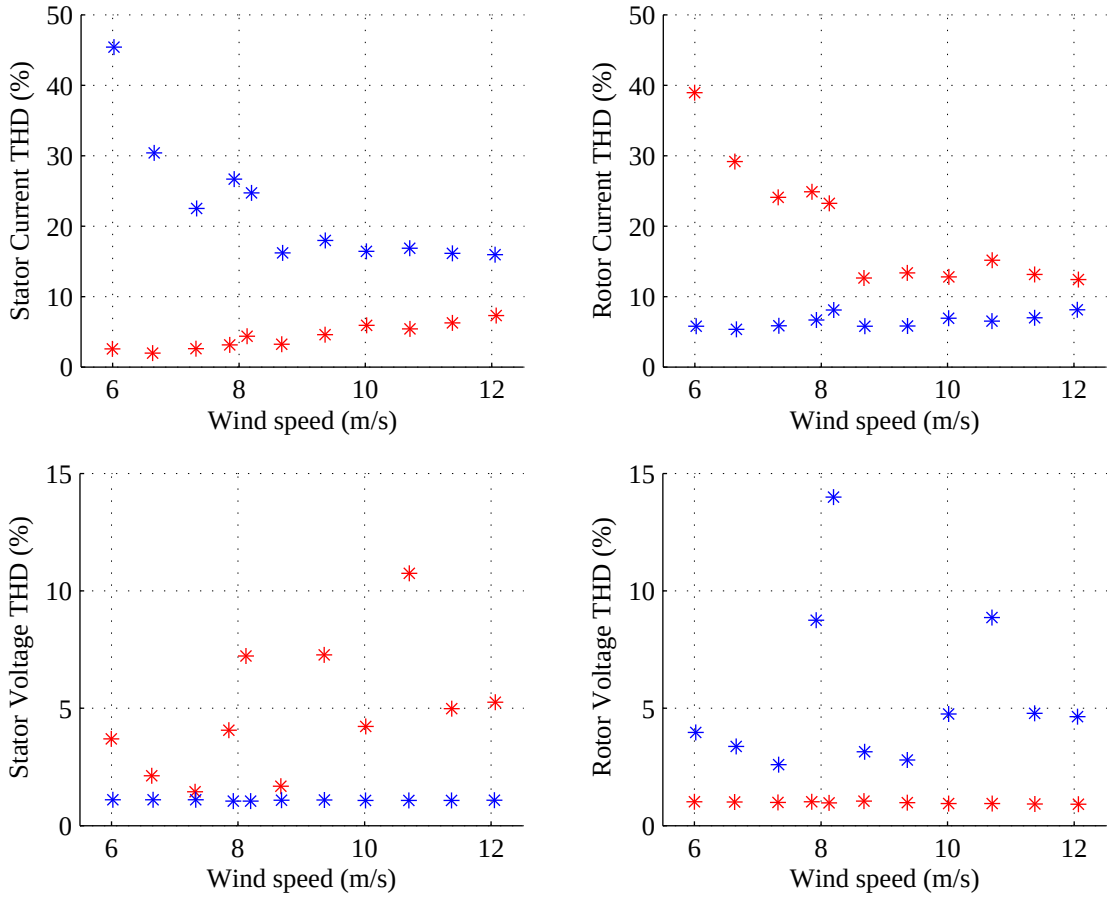

Figure 3.8 Voltage and current total harmonic distortion. (Rotor-tied: red, stator-tied: blue.)

However, these harmonics are highly machine-dependent, and it is important to note that the machine being tested here is not designed for a wind turbine application, nor are the windings of "inverter-grade" quality. A snapshot of the rotor and stator currents for operating at a wind speed of 10 m/s in the rotor-tied configuration is shown in Fig. 3.9.

A Weibull probability density function is used to describe the annual variation of wind speed [8], [9]

$$f(v_w) = \frac{k}{c}\left(\frac{v_w}{c}\right)^{k-1} e^{-(v_w/c)^k} \tag{3.3}$$

where c is the scale factor, k is the shape factor, and v_w is the wind speed. Here, we assume values of $k = 2$ and $c = 8.3$ m/s; the resulting average wind speed is $\bar{v}_w = 7.4$ m/s. The

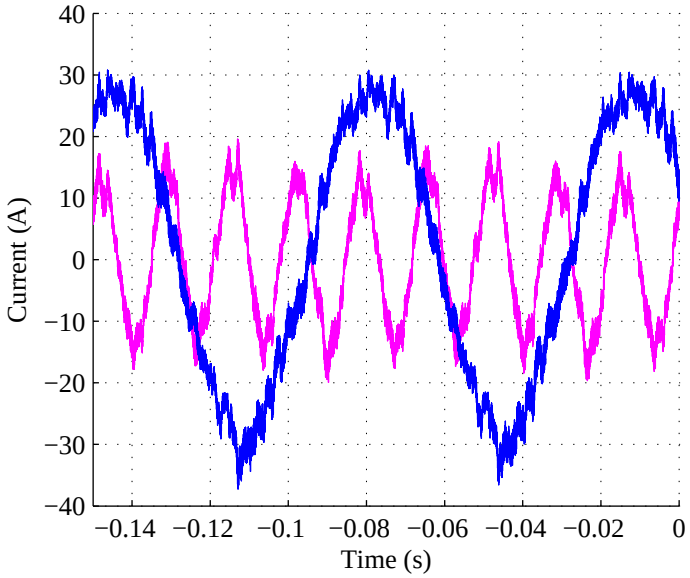

Figure 3.9 Rotor (magenta) and stator (blue) current while operating at 1500 rpm, with $T_{\text{shaft}} = 28$ Nm and $Q_r = 0$ VAR.

expected annual energy generation for each configuration is computed by

$$E_{\text{gen}} = 8760 \int_{v_w^{\text{in}}}^{v_w^{\text{out}}} P_{\text{gen}}(v_w) f(v_w) dv_w \tag{3.4}$$

where $P_{\text{gen}}(v_w)$ is a cubic polynomial curve that fits the measured total generation measurements. The cut-in wind speed is taken to be $v_w^{\text{in}} = 6$ m/s, and the cut-out wind speed is taken to be $v_w^{\text{out}} = 25$ m/s. For wind speeds beyond rated value, approximately 12 m/s, the machine operates at rated power. The power vs. wind speed curves are shown in Fig. 3.10. Under the assumed wind resource, we expect the rotor-tied configuration to result in an annual energy generation of 17.87 MWh, compared to 16.46 MWh in the stator-tied; this is an 8.5% increase. Extrapolating this efficiency improvement to a multi-MW machine could mean significant energy savings.

3.5 Conclusions

An alternative connection topology for the DFIG has been experimentally tested and compared to the conventional one. Steady-state tests were performed for both configurations at operating conditions encountered in variable-speed wind turbines. The results indicate that

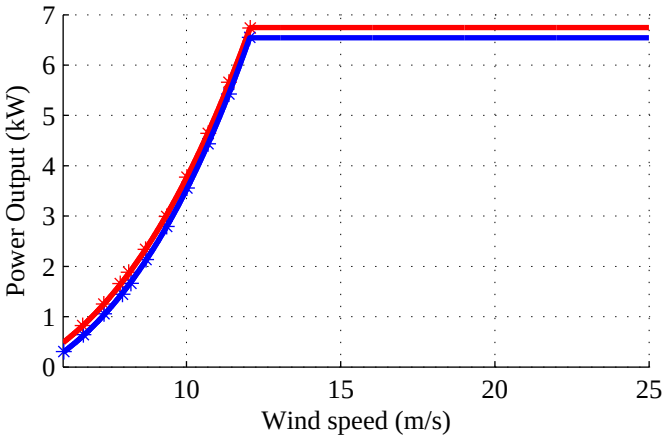

Figure 3.10 Power curves over the operating wind speed range. (Rotor-tied: red, stator-tied: blue.)

the rotor-tied configuration is preferred in terms of energy conversion efficiency, and can offer significant energy savings. This conclusion is also supported by theoretical analysis, but further work is necessary to better understand why this is the case.

Operation and control of the machine is very similar in the new configuration, and does not require additional components. However, the effects of additional power flow through the slip ring and brushes could warrant attention.

CHAPTER 4. SUMMARY AND DISCUSSION

4.1 Contributions

This thesis explored operation of a wind energy conversion system equipped with a DFIG in an alternative configuration, for the purpose of increasing energy conversion efficieny. Significant contributions and conclusions are as follows:

1. An alternative connection strategy which allows one to operate a DFIG based wind turbine with greater efficiency than the current art offers has been proposed, analyzed, and validated. We determined a feasible operating region (speed and slip) based on the electronic power converter ratings. By developing a general relationship of rotor and stator core volumes, we were able to analyze the core loss under different operating conditions. Theoretical results indicate a reduction of core loss due to hysteresis in the proposed configuration, and results in increased efficiency. With statistical wind speed characteristics, an increase in annual energy generation was observed.

2. Proportional plus integral (PI) controllers were developed to control the stator current, rotor reactive power, and electromagnetic torque when operating the DFIG in the rotor-tied configuration. A transfer function with pole-placement method was used to design the controllers. The equations associated with the controllers are found to be very similar in both configurations, with the possibility to modify existing controllers for use in the new configuration.

3. A prototype back-to-back power converter and control system was built and used for testing a 7.5 kW DFIG in the laboratory. The test stand is capable of testing the machine at various voltage, speed, torque, and reactive power conditions. No special equipment is

required to run this test stand in the new configuration. Tests performed on the machine have proven that the proposed rotor-tied configuration is indeed more efficient than the popular stator-tied configuration, and could result in an 8.5% annual energy generation increase.

4.2 Future Work

From the results observed so far, there appears to be a need for work done in the following areas:

1. At low speed and low torque, there is a lot of harmonic content in the stator currents. These are believed to be due to machine slot harmonics and space vector modulation harmonics, and can have a considerable effect on the efficiency of the machine. At high speed and high torque, these harmonics are greatly reduced, and their effects become less dominant. It would be interesting to analyze the core loss in a more detailed manner, in which switching harmonics and slot harmonics can be accurately predicted. To capture the effects of machine harmonics, more advanced machine models are required. It would also be beneficial if one could find a way to reduce the current THD in general, perhaps through adopting alternative power electronic converter topologies and control algorithms.

2. With an overall reduction of losses, it is expected that the machine will run at a lower average temperature, which could impact the working lifetime of the machine. Most machines, including the one tested in the laboratory, have a temperature sensor. However, the temperature in all regions of the machine is not expected to have decreased. While the results show that the core loss has decreased, they also show that the resistive losses have increased. To understand the temperature variations within the machine, it is necessary to know the precise location of the sensor. From the results obtained so far, it is expected that the stator copper temperature has increased, and the stator iron core temperature has decreased. Similarly, we expect the rotor copper temperature has decreased, while the rotor iron core temperature has increased. To this end, it would be interesting to

design and build a motor that has an array of temperature sensors placed throughout the machine.

3. DFIGs available today are not designed specifically for the operating in the rotor-tied configuration. Operating in this unintended fashion begs the question of whether there are additional mechanical phenomena that must be considered. Temperature variations can result in different impacts depending on the physical location within the machine. For instance, a rise in copper temperature can lead to premature failure of the insulation, and a rise in temperature of the iron can result in increased expansion and fatigue. While operating in the rotor-tied configuration, it could be the case that the stator windings cannot handle the increased temperature, or that the rotor structure cannot handle the additional heat generated in the rotor core. Additional studies are required to understand the impacts this new configuration might have on the mechanical structure of the machine.

4. It is probably necessary to re-design the slip ring if the machine is to be operated in the rotor-tied configuration. The slip-ring is intended to only handle one third of the maximum power. However, in the rotor-tied configuration, it must handle double that. While no adverse effects were observed during experimentation, it is likely that the brush and ring contact surface could not sustain operation for an extended period of time. More detailed studies regarding slip-ring and brush power handling capabilities could be conducted to determine a brush/slip ring configuration suitable to handling two-thirds of the maximum power. An increase in the brush/ring contact surface area is expected.

5. Experiments should be performed on multi-MW machines to determine if this technology is suitable for commercial use. Based on the assumptions made in this work, it is likely that these larger machines will also experience efficiency improvements when operated in the new configuration. The potential increase in energy generation deems additional large-scale studies necessary.

APPENDIX A. DFIG AND FILTER REACTOR PARAMETERS

A.1 DFIG Parameters

The machine studied is a wound rotor induction machine (part no: YZR 160M2-6). This is a 6-pole machine, and has the following ratings: $f = 60$ Hz, $V_r = 195$ V, $V_s = 208$ V, $I_s = 31$ A, $I_r = 26$ A, and $P_{\text{shaft}} = 7.5$ kW.

The per-phase equivalent circuit parameters were obtained in conformance with IEEE Standard 112-2004 [17]. Tests include a dc resistance, no-load, locked-rotor, and full-load test. Details regarding these tests are not provided here. The value for equivalent core resistance obtained by this method was neglected, as core loss is considered by (3.2). When the machine is connected in Δ-Y, the per-phase equivalent circuit machine parameters are $r_s = 15.93$ mΩ, $r'_r = 8.69$ mΩ, $L_{ls} = 1.9$ mH, $L'_{lr} = 1.9$ mH, and $L_M = 17.1$ mH, with a turns ratio of $N = 1.067$. Brush and slip ring resistances are negligible. The equivalent circuit is shown in Fig. A.1.

A.2 Filter Reactor Parameters

The reactor coupling the GSC to the grid is a three-phase reactor (MTE RL-00803), with each phase wound on a common E-type iron laminate core. The reactor has the following ratings: $V = 208$ V, $I = 12$ A, and $f = 60$ Hz.

The *abc* voltage equations for this type of reactor are

$$v_{an}(t) = R_a i_a(t) + L_a \frac{di_a(t)}{dt} + M_{ab} \frac{di_b(t)}{dt} + M_{ac} \frac{di_c(t)}{dt} \tag{A.1}$$

$$v_{bn}(t) = R_b i_b(t) + M_{ba} \frac{di_a(t)}{dt} + L_b \frac{di_b(t)}{dt} + M_{bc} \frac{di_c(t)}{dt} \tag{A.2}$$

$$v_{cn}(t) = R_c i_c(t) + M_{ca} \frac{di_a(t)}{dt} + M_{cb} \frac{di_b(t)}{dt} + L_c \frac{di_c(t)}{dt}. \tag{A.3}$$

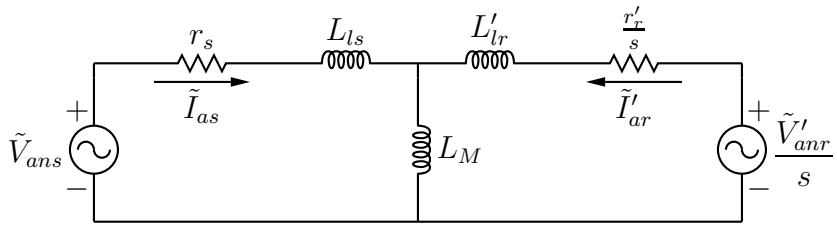

Figure A.1 Per-phase equivalent circuit of the doubly-fed induction generator.

When written in matrix form $\boldsymbol{v}(t) = R\boldsymbol{i}(t) + \boldsymbol{L}\frac{d\boldsymbol{i}(t)}{dt}$, the inductance matrix is

$$L = \begin{bmatrix} L_a & M_{ab} & M_{ac} \\ M_{ba} & L_b & M_{bc} \\ M_{ca} & M_{cb} & L_c \end{bmatrix} \tag{A.4}$$

Because of the asymmetrical flux paths within the core, the mutual inductances between phases have different values. In this design, the current through the reactor will be controlled in the synchronous qd reference frame. It is sufficient for these purposes to neglect the mutual inductance, and assume equal values for inductances L_a, L_b, and L_c. Then, the abc circuit is easily transformed to the qd circuit of Fig. A.2 (shown for the arbitrary reference frame). If the core is assumed symmetrical, the values of L_q and L_d are identical. However, the reactor core considered here is not, and thus, the values of L_q and L_d will have different values. Parameters R, L_q, and L_d are determined through tests performed in the stationary qd reference frame, and due to the asymmetry of the core, are specific to a certain phase designation (i.e., which terminals are labeled a, b, and c). These parameters are obtained by tests detailed here.

A.2.1 Resistance Test

The per-phase resistance, R, is obtained by applying a dc voltage, V, from one phase to another and measuring the current, I.

$$R = \frac{V}{2I} \tag{A.5}$$

The average of all phase-to-phase tests is taken as the per-phase resistance. From the transformation of abc to qd [4], the q- and d-axis resistances are equal to the per-phase resistance. The value is found by this test is $R = 89.1$ mΩ.

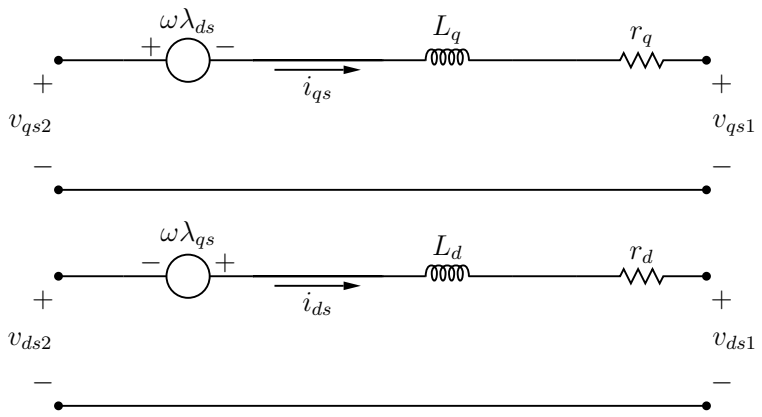

Figure A.2 Filter reactor qd circuit; shown in the arbitrary reference frame.

A.2.2 Steady-State Inductance Test

In steady-state, the reactor can be modeled by a resistance in series with an inductance. The inductance value has been provided by the manufacture, and is specified as 5 mH. The steady-state test performed here will put a value to both the resistance and inductance.

The primary side of the reactor is connected to the terminals of the grid via a three-phase variac. The secondary side of the reactor is connected to a 4.7 Ω three-phase Y-connected resistance, to limit the current. Applying a balanced three-phase voltage source induces a current with specific magnitude and phase-angle. The voltage and current phasors, $\tilde{V}$ and $\tilde{I}$, associated with each phase of the RL circuit are measured with an oscilloscope. The per-phase steady-state impedance, $Z_\phi = R_\phi + j\omega_g L_\phi$ is found for each phase as

$$Z_\phi = \frac{\tilde{V}}{\tilde{I}}. \tag{A.6}$$

where ω_g is the angular frequency of the grid source. The values of R and L used in the per-phase equivalent-circuit are taken as the average values of all three phases, and are $R = 133$ mΩ and $L = 4.5$ mH.

A.2.3 Dynamic *qd* Tests

The reactor dynamic response can be modeled by the qd circuit of Fig. A.2. The qd inductances are determined through voltage-step tests. The resistance can also be calculated during this test.

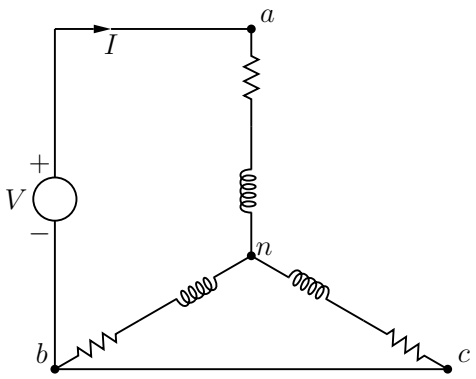

Figure A.3 Test configuration for obtaining the filter reactor inductance, L_q.

The reactor terminals of one side are connected in Y-configuration, and the terminals of the other side are designated as a, b, and c. Since the reactor core is non-symmetrical, it is not likely that the q- and d-axis inductances will have the same value. Because of this, it is important that phase designation be maintained while operating, as is assigned during testing.

Under the assumptions stated earlier regarding mutual inductances, the voltage equations in the arbitrary qd reference frame are

$$v_q(t) = r_q i_q(t) + \omega\,(L_q)\,i_d(t) + (L_q)\,\frac{d}{dt} i_q(t) \tag{A.7}$$

$$v_d(t) = r_d i_d(t) - \omega\,(L_d)\,i_d(t) + (L_d)\,\frac{d}{dt} i_q(t). \tag{A.8}$$

If the reactor phase designation is changed, the parameters must be re-measured for that configuration. In the stationary reference frame, $\omega = 0$, so these become

$$v_q(t) = r_q i_q(t) + (L_q)\,\frac{d}{dt} i_q(t) \tag{A.9}$$

$$v_d(t) = r_d i_d(t) + (L_d)\,\frac{d}{dt} i_q(t). \tag{A.10}$$

To find the value of L_q, a voltage step is applied to the q-axis. This is done by applying a voltage between phases a and b, while phase c is short circuited to phase b, as depicted in Fig. A.3. The transformation of abc to qd yields

$$v_q = \frac{2}{3} V \tag{A.11}$$

$$v_d = 0 \tag{A.12}$$

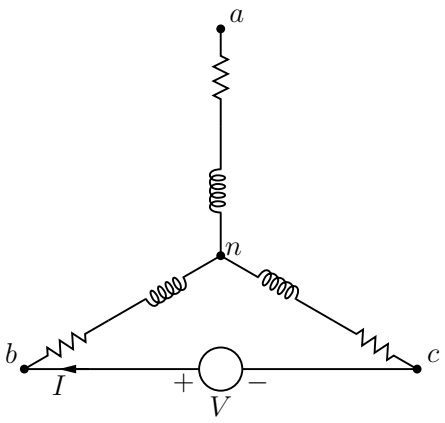

Figure A.4 Test configuration for obtaining the filter reactor inductance, L_d.

and

$$i_q = I \tag{A.13}$$

$$i_d = 0 \tag{A.14}$$

where V is the applied source voltage and I is the source current. The q-axis inductance is obtained by

$$L_q = \frac{\int_{t_0}^{T} v_q(t) - r_q i_q(t) dt}{i_q(T)} \tag{A.15}$$

where r_q is found first, using the steady-state values of the measured voltage and current. It is important to remove the dc offset from the measured values; this is computed by the average pre-step measurements.

To find the value of L_d, a voltage step is applied to the d-axis. This is done by applying a voltage step between phases b and c, while phase a is open-circuited, as depicted in Fig. A.4. The transformation of abc to qd yields

$$v_q = 0 \tag{A.16}$$

$$v_d = -\frac{\sqrt{3}}{3} V \tag{A.17}$$

and

$$i_q = 0 \tag{A.18}$$

$$i_d = \frac{-2\sqrt{3}}{3} I. \tag{A.19}$$

The d-axis inductance is obtained by

$$L_d = \frac{\int_{t_0}^{T} v_d(t) - r_d i_d(t) dt}{i_d(T)} \tag{A.20}$$

where r_d is found in a similar manner to r_q.

The values obtained by the qd step tests are $r_q = 94.9$ mΩ, $r_d = 89.5$ mΩ, $L_q = 4.4$ mH, and $L_d = 4.7$ mH.

APPENDIX B. DFIG STEADY-STATE CIRCUIT SOLUTION

In the rotor-tied configuration, the DFIG steady-state per-phase equivalent circuit, shown in Fig. B.1, is solved using an iterative process to satisfy the conservation of power. For a given value of slip, s, the rotor reactive power is controlled to $Q_r = 0$ VAR. Shaft power and terminal power are defined positive as entering the machine. So, from the physics of the machine [4], the per-phase rotor real power, P_r, can be estimated by

$$P_r \approx \frac{-P_m}{3\left(1-\frac{1}{s}\right)} \tag{B.1}$$

where P_m is the amount of extractable mechanical power provided by the wind, and has value

$$P_m = 0.5\rho C_p A v_{\text{wind}}^3. \tag{B.2}$$

where ρ is the density of the air, A is the swept area, and C_p is the wind turbine's performance coefficient.

Knowing the magnitude and angle of the stator-referred grid voltage phasor, $\tilde{V}_r'$, as well as the grid frequency, f_r, the per-phase equivalent circuit can be solved. The estimated per-phase rotor apparent power is

$$S_r = P_r + jQ_r \tag{B.3}$$

which leads to the stator-referred rotor current

$$\tilde{I}_r' = \left(\frac{S_r}{\tilde{V}_r'}\right)^* \tag{B.4}$$

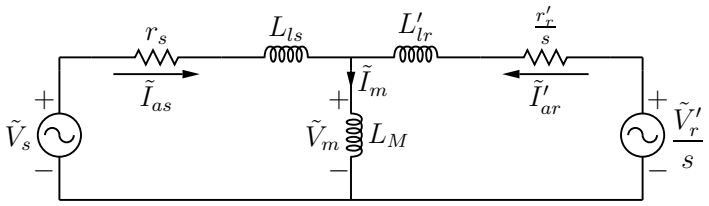

Figure B.1 Per-phase equivalent circuit of the DFIG.

where * denotes the conjugate operator. All other circuit quantities are computed as

$$\tilde{V}_m = \tilde{V}'_r + \tilde{V}'_r \left(\frac{1-s}{s}\right) - r'_r \left(\frac{1-s}{s}\right) \tilde{I}'_r - \left(r'_r + j\omega_e L'_{lr}\right) \tilde{I}'_r \tag{B.5}$$

$$\tilde{I}_m = \frac{\tilde{V}_m}{j\omega_e L_M} \tag{B.6}$$

$$\tilde{I}_s = \tilde{I}_m - \tilde{I}'_r \tag{B.7}$$

$$\tilde{V}_s = \tilde{V}_m + \tilde{I}_s \left(r_s + j\omega_e L_{ls}\right) \tag{B.8}$$

where ω_e varies with slip as

$$\omega_e = 2\pi \left(\frac{f_r}{s}\right). \tag{B.9}$$

Then, the per-phase stator terminal real power is computed as

$$P_s = \mathrm{Re}\left\{\tilde{V}_s \tilde{I}_s^*\right\}. \tag{B.10}$$

Ohmic losses are computed by

$$P_{\text{ohmic}} = \tilde{I}'^2_r r'_r + \tilde{I}'^2_s r_s \tag{B.11}$$

and core loss due to magnetic hysteresis is computed by

$$P_{\text{core},x} = \left(k_h B^n_{\text{max},x} f_x\right) \left(\text{Vol}_x\right) \left(\gamma\right) \tag{B.12}$$

for each region x and corresponding frequency of magnetization f_x.

Conservation of power must be satisfied. The power provided by the wind and the stator and rotor terminal powers are defined positive as entering the machine. Losses are defined positive as exiting the machine. Thus, error is computed by

$$\text{Err} = P_m - 3P_{\text{ohmic}} - \sum_x P_{\text{core},x} + 3P_r + 3P_s. \tag{B.13}$$

If the error is outside of a chosen tolerance (e.g. Tol = 0.1 W), the estimated rotor terminal real power is updated by

$$P_r \approx P_r - (\text{Tol})\,(\text{Err})\,. \tag{B.14}$$

When the solution has converged, the analysis is complete.

APPENDIX C. SYSTEM CONTROLS

C.1 Grid-Side Converter

In the rotor-tied configuration, the stator of the machine is coupled to the grid via a back-to-back power electronic converter. The same back-to-back converter is used in the stator-tied configuration, and is composed on two independent power electronic converters. The machine-side converter (MSC) is connected to the non-grid connected side of the DFIG, and the grid-side converter (GSC) is coupled to the grid via a three-phase filter inductor. The MSC and GSC are connected to each other via a dc-link.

The GSC regulates the dc-bus voltage to remain at a constant predefined value, and controls the reactive power injected to the grid at the filter reactor terminals. The reactor currents are controlled in the synchronous qd reference frame by PI controllers, with command values generated by PI controllers that regulate the dc-link voltage and grid reactive power injection. The reactive power at the filter's reactor-to-grid terminals is controlled to 0 VAR.

A three-phase diagram and per-phase equivalent circuit diagram are shown in Fig. C.1. All control will be done in the synchronous qd reference frame, denoted by superscript e; steady-state values are dc. The three-phase circuit is transformed to the arbitrary qd reference frame as described in [4]. The transformation is of the form

$$f_{qd0s} = K_s f_{abcs} \tag{C.1}$$

where

$$K_s = \frac{2}{3}\begin{bmatrix} \cos(\theta) & \cos\left(\theta - \frac{2\pi}{3}\right) & \cos\left(\theta + \frac{2\pi}{3}\right) \\ \sin(\theta) & \sin\left(\theta - \frac{2\pi}{3}\right) & \sin\left(\theta + \frac{2\pi}{3}\right) \\ \frac{1}{2} & \frac{1}{2} & \frac{1}{2} \end{bmatrix} \tag{C.2}$$

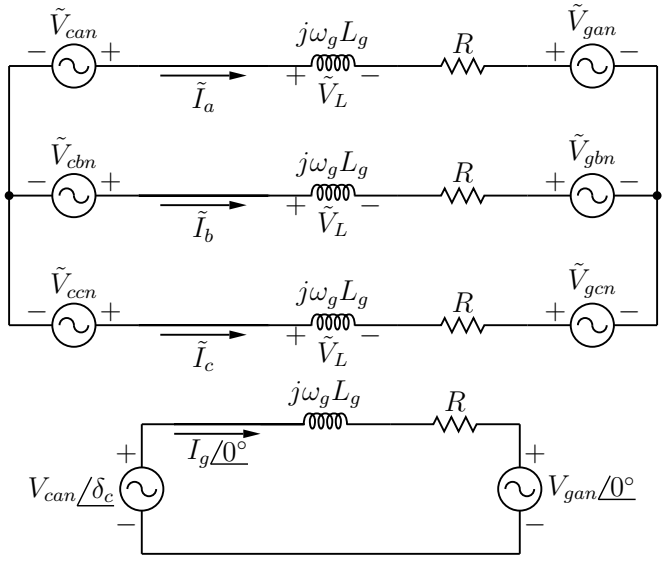

Figure C.1 Three-phase and per-phase circuit diagrams of the GSC coupled with the grid.

$$\omega = \frac{d\theta}{dt}. \tag{C.3}$$

Here, ω is the angular velocity of the reference frame. Subscript s denotes the arbitrary reference frame. The inverse transformation is

$$f_{abcs} = K_s^{-1} f_{qd0s} \tag{C.4}$$

where

$$K_s^{-1} = \begin{bmatrix} \cos(\theta) & \sin(\theta) & 1 \\ \cos\left(\theta - \frac{2\pi}{3}\right) & \sin\left(\theta - \frac{2\pi}{3}\right) & 1 \\ \cos\left(\theta + \frac{2\pi}{3}\right) & \sin\left(\theta + \frac{2\pi}{3}\right) & 1 \end{bmatrix}. \tag{C.5}$$

Transforming the GSC terminal voltage to the arbitrary qd reference frame yields q- and d-axis voltages v_{cqs} and v_{cds}, and transforming the grid terminal voltage yields v_{gqs} and v_{gds}.

For a three-phase inductive element with per-phase series inductance L_g, the abc voltage across the inductance is

$$v_{abcs} = p\lambda_{abcs} \tag{C.6}$$

where λ_{abcs} is the flux linkage of the inductive element, and p is the time derivative operator $\frac{d}{dt}$. Transforming this equation to the arbitrary reference frame, as detailed in Appendix E.2,

results in the q- and d-axis voltages across the inductor

$$v_{qs} = \omega\lambda_{ds} + p\lambda_{qs} \tag{C.7}$$

$$v_{ds} = -\omega\lambda_{qs} + p\lambda_{ds} \tag{C.8}$$

$$v_{0s} = p\lambda_{0s} \tag{C.9}$$

where neglecting mutual inductance,

$$\lambda_{qs} = L_g i_{qs} \tag{C.10}$$

$$\lambda_{ds} = L_g i_{ds} \tag{C.11}$$

$$\lambda_{0s} = L_g i_{0s}. \tag{C.12}$$

Thus, the voltage across the inductance in the arbitrary qd reference frame is

$$v_{qs} = \omega L_g i_{ds} + L_g p i_{qs} \tag{C.13}$$

$$v_{ds} = -\omega L_g i_{qs} + L_g p i_{ds} \tag{C.14}$$

$$v_{0s} = L_g p i_{0s}. \tag{C.15}$$

The arbitrary qd circuit, which is valid in both steady-state and transient, for the reactor filter coupling the GSC with the grid is shown in Fig. C.2. The GSC terminal voltage is related to the grid terminal voltage by

$$v_{cqs} = v_{gqs} + Ri_{qds} + L_g p i_{qs} + \omega L_g i_{ds} \tag{C.16}$$

$$v_{cds} = v_{gds} + Ri_{qds} + L_g p i_{ds} - \omega L_g i_{qs} \tag{C.17}$$

$$v_{c0s} = v_{g0s} + Ri_{qds} + L_g p i_{0s}. \tag{C.18}$$

C.1.1 Steady-State Conditions And Device Selection

Current is defined positive into the grid terminals (out of the converter). Therefore, real and reactive power are also defined positive entering the grid terminals. The PLL measures the grid voltage in the synchronous reference frame, and aligns the reference frame such that

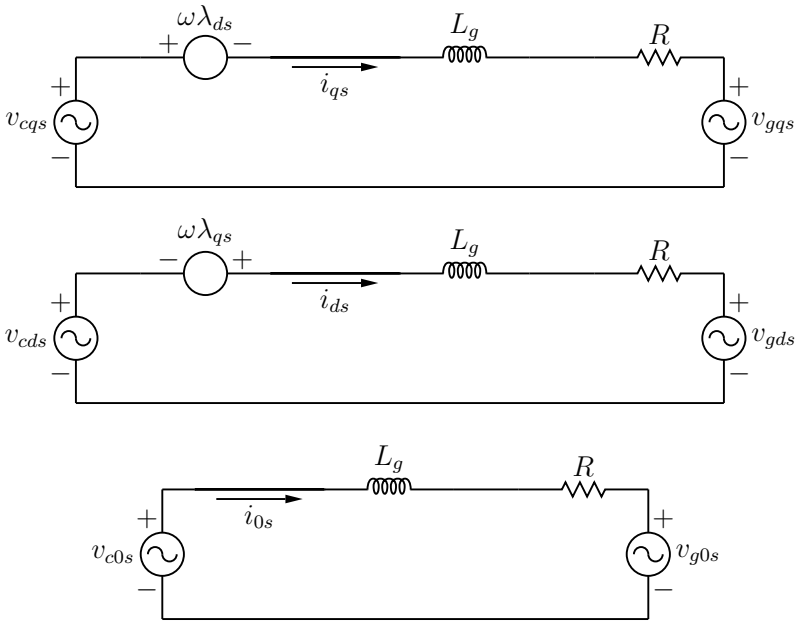

Figure C.2 Arbitrary reference frame qd circuit of the GSC coupled with the grid.

$v^e_{gd} = 0$. This makes the real and reactive power at the grid terminals become

$$P_g = \frac{3}{2} v^e_{gq} i^e_{gq} \tag{C.19}$$

$$Q_g = \frac{3}{2} v^e_{gq} i^e_{gd}. \tag{C.20}$$

The amount of real power delivered to the grid is the result of controlling the dc-link voltage. For example, as real power is removed from the machine, the dc-link voltage will tend to rise as more energy is stored in the capacitors. The controller then increases the amount of power delivered to the grid, and the dc-link voltage tends to decrease. The desired reactive power injection will be $Q^*_g = 0$ for unity power factor operation; terminal voltage regulation via reactive power support is not performed.

For the sake of choosing an inductor value, it is useful to consider the maximum steady-state converter voltage magnitude. This voltage will be generated using SVM, and corresponds to a minimum dc-link voltage that must be maintained during normal operation. Since the system is design such that the converter handles 1/3 of the maximum power generation, the maximum power delivered to the grid via the GSC, in either the stator-tied or rotor-tied configuration, is $P_{g\max} = 2.5$ kW for the system under test. The GSC is designed for the stator-tied config-

uration, since this is the popular configuration. The GSC will then be tested in the rotor-tied configuration, without special design considerations.

During steady-state, with a grid voltage of $v_{gq}^{e} = 169.83$ V and synchronous reference frame speed of $\omega_e = 2\pi 60$ rad/s, the maximum q-axis current is

$$i_{gq\max}^{e} = \frac{2}{3}\left(\frac{P_{g\max}}{v_{gq}^{e}}\right) = 9.81 \text{ A}. \tag{C.21}$$

The required maximum steady-state converter voltage is

$$v_{cq\max}^{e} = v_{gq}^{e} + Ri_{gq\max}^{e} + \omega_e L_g i_{gd\max}^{e} \tag{C.22}$$

$$v_{cd\max}^{e} = v_{gd}^{e} + Ri_{gd\max}^{e} - \omega_e L_g i_{gq\max}^{e}. \tag{C.23}$$

The converter voltage space vector will have a maximum magnitude of

$$V_{cp\max} = \sqrt{v_{cq\max}^{e2} + v_{cd\max}^{e2}}. \tag{C.24}$$

The minimum dc-link voltage required for SVM is

$$V_{dc\min} = \sqrt{3} V_{cp\max}. \tag{C.25}$$

It is desirable to find a range of inductances that satisfy the design before searching for parts to purchase. The maximum inductance is chosen to ensure that the maximum desired converter voltage can be generated using the specified dc-link voltage. First, it is decided that the dc-link voltage will be 12% larger than the rectified grid voltage. In the stator-tied configuration, the line-to-line grid voltage is $V_{\text{grid}} = 208$ V, making the desired dc-link voltage be $V_{dc} = 330$ V. The maximum converter voltage space vector that can be generated will have a magnitude of

$$V_{cp\max} = \frac{V_{dc}}{\sqrt{3}} = 190.53 \text{ V}. \tag{C.26}$$

Neglecting the resistive voltage drop, the corresponding maximum q- and d-axis voltages that must be generated by the converter are

$$v_{cq\max}^{e} = 169.83 \text{ V} \tag{C.27}$$

$$v_{cd\max}^{e} = \omega_e L_{g\max} i_{gq\max}^{e}. \tag{C.28}$$

so using (C.26)

$$|v^e_{cd\max}| = \sqrt{V^2_{cp\max} - v^{e2}_{cq\max}} \tag{C.29}$$

which leads to

$$L_{g\max} = \frac{\sqrt{V^2_{cp\max} - v^2_{cq\max}}}{\omega_e i^e_{gq\max}} = 23.3 \text{ mH}. \tag{C.30}$$

Now, assuming an overload current of $5 \times i^e_{gq\max}$ is allowed for short durations, this becomes

$$L_{g\max} = \frac{\sqrt{V^2_{cp\max} - v^{e2}_{cq\max}}}{5\omega_e i^e_{gq\max}} = 4.7 \text{ mH}. \tag{C.31}$$

The maximum series inductance allowed is approximately 5 mH when using a dc-link voltage of 330 V.

The grid-coupling circuit is essentially a first-order low-pass RL filter. It is useful to consider the corner frequency, as it is necessary to attenuate high frequency components. The cutoff frequency of an RL filter is

$$f_c = \frac{R_{eq}}{2\pi L_g}. \tag{C.32}$$

At the maximum power condition, the power delivered to the grid, per phase, is

$$P_\phi = \frac{P_{g\ \max}}{3} = \frac{V_g^2}{R_{eq}} \tag{C.33}$$

where R_{eq} is the equivalent grid resistance at this condition, and V_g is the rms line-to-neutral voltage. For the system here,

$$R_{eq} = \frac{3V_g^2}{P_{g\ \max}} = 17.3\ \Omega. \tag{C.34}$$

Placing the cutoff frequency one decade below the switching frequency (assumed to be 5 kHz) yields a minimum inductance of

$$L_{g\min} = \frac{R_{eq}}{2\pi\left(\frac{f_{sw}}{10}\right)} = 5.5 \text{ mH}. \tag{C.35}$$

If the switching frequency is increased to 10 kHz, the minimum inductance is reduced to $L_{g\min} = 2.8$ mH. A three-phase reactor that is commercially available is chosen to be

$$L_g = 5 \text{ mH}. \tag{C.36}$$

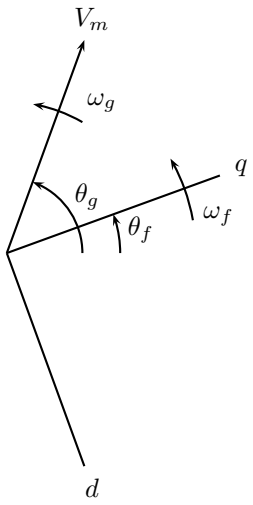

Figure C.3 Vector relationships for the PLL

With this inductance, and (C.25), the dc-link voltage required for maximum power operation is $V_{dc\min} = 295.9$ V. During a current overload of 5 times the nominal value, choosing a 5 mH inductance will require a dc-link voltage of 334 V. This will be considered an acceptable design.

C.1.2 Phase-Locked-Loop

A synchronous reference frame phase-locked-loop (SRF-PLL) is used to measure the grid voltage vector magnitude and position [18]. The grid voltage vector is defined here to have magnitude V_m and angular frequency ω_g. At any moment in time, the vector is positioned at θ_g. The rotating reference frame has angular frequency ω_f. At any moment in time, the reference frame is positioned at θ_f. The projection of the grid vector onto the rotating reference frame yields qd components

$$v_q = V_m \cos(\theta_g - \theta_f) \tag{C.37}$$

$$v_d = -V_m \sin(\theta_g - \theta_f) \tag{C.38}$$

It is clear that when $v_d = 0$, $\theta_f = \theta_g$; the q-axis of the rotating reference frame is aligned with the grid voltage vector as illustrated in Fig. C.3.

A PI controller works to keep the angle of the rotating reference frame aligned with the voltage vector. The actual d-axis voltage is compared to the desired value of $v_d^* = 0$. When

$v_d > v_d^* = 0$, the reference frame needs to slow down. When $v_d < v_d^* = 0$, the reference frame needs to speed up. The difference is used to adjust the frequency of the rotating reference frame, via PI control.

The measured *abc* voltages are transformed to the rotating reference frame. Due to noise induced by power electronic switching events, it is necessary to filter the d-axis voltage before being used in the comparison. If the voltage is not filtered, the switching noise is amplified by the proportional gain, and appears in the measured grid speed ω_e. The PLL is designed to be relatively slow, to track the fundamental component of the grid. It is not intended to be used for applications such as fault-ride-through or terminal voltage regulation, which requires fast tracking.

It is useful to find the angle of the grid voltage vector in terms of the d-axis voltage. Using the small angle approximation for small deviations of grid speed, the d-axis voltage deviation is

$$\Delta v_d = -V_m \left(\Delta\theta_g - \theta_f\right). \tag{C.39}$$

The grid voltage vector position is taken as the reference point, so $\Delta\theta_g$ is taken to be zero, and the deviation will appear in the reference frame angle, $\Delta\theta_f$. Then, rearranging (C.39) yields the angle deviation of the reference frame

$$\Delta\theta_f = \frac{\Delta v_d}{V_m}. \tag{C.40}$$

For small deviations of the grid speed from nominal, the reference frame angle is

$$\theta_f = \int 2\pi 60 \text{ dt} + \frac{v_d}{V_m}. \tag{C.41}$$

Assuming positive values for parameters K and τ, the commanded angle of the reference frame is defined to be

$$\theta_f^* = \int \left(2\pi 60 + \left(v_d^* - v_d\right) K \left(1 + \frac{1}{\tau s}\right)\right) \, dt. \tag{C.42}$$

Equating C.41 and C.42 in the frequency domain [19] yields the transfer function

$$\frac{v_d}{v_d^*} = \frac{KV_m\left(s + \frac{1}{\tau}\right)}{s^2 + KV_m s + \frac{KV_m}{\tau}}. \tag{C.43}$$

The system has one zero located at

$$s_z = \frac{-1}{\tau}. \tag{C.44}$$

The system has two poles located at

$$s_{p1,2} = \frac{-KV_m \pm \sqrt{K^2V_m^2 - \frac{4KV_m}{\tau}}}{2}. \tag{C.45}$$

When the radicand equals zero, the poles are located at

$$s_{p1,2} = \frac{-KV_m}{2}. \tag{C.46}$$

The center of the poles is placed by choosing the value of K to be

$$K = \frac{-2s_{p1,2}}{V_m}. \tag{C.47}$$

Making the radicand equal to zero results in critical damping. Additional damping can be added by a factor c multiplying the value of τ. When $c > 1$, the poles will be moved by equal amounts, and in opposite directions, from the central location, both by equal amounts. When $0 < c < 1$, the poles will have an imaginary component. The value of τ is chosen to make the radicand equal to zero, so

$$\tau = \frac{4}{KV_m}. \tag{C.48}$$

After adjusting the damping, the zero is located at

$$s_z = -\frac{1}{c\tau} \tag{C.49}$$

and the poles are located at

$$s_{p1,2} = \frac{-KV_m \pm \sqrt{K^2V_m^2 - \frac{4KV_m}{c\tau}}}{2}. \tag{C.50}$$

The resulting qd voltages are filtered through a first order filter with corner frequency placed at $f_{cvqd} = \frac{f_{\text{sw}}}{10000}$, making the measured values nearly dc, and equal to the grid fundamental component.

C.1.3 Current Control

The *abc* currents are measured and transformed to the rotating reference frame. The *qd* grid currents are controlled by PI controllers. The output of the controllers are the q- and d-axis voltage commands in the synchronous reference frame.

C.1.3.1 q-Axis Control

Voltage equation (C.16) relates the q-axis current to the q-axis converter voltage; it is restated here for the synchronous reference frame; the time-domain has been transformed to the s-domain.

$$v_{cq}^{e} = Ri_{gq}^{e} + L_g s i_{gq}^{e} + \omega_e L_g i_{gd}^{e} + v_{gq}^{e} \tag{C.51}$$

The q-axis voltage commanded by the controller is defined here to be composed of the voltage present in the circuit which is independent of the controlled q-axis current, plus a term which depends on the PI controlled q-axis current, as

$$v_{cq}^{e*} = \left(v_{gq}^{e} + \omega_e L_g i_{gd}^{e}\right) + K\left(1 + \frac{1}{\tau s}\right)\left(i_{gq}^{e*} - i_{gq}^{e}\right) \tag{C.52}$$

where i_{gq}^{e*} is the desired q-axis current, i_{gq}^{e} is the actual q-axis current, and K and τ are parameters of the PI controller.

The microcontroller fundamental step time, rise/fall times of the power devices, and any other propagation delays are considered negligibly small. Therefore, these time delays are not considered in the PI controller design. The GSC is assumed to generate an actual voltage which is equal to the commanded voltage. Equating (C.51) and (C.52) in the frequency domain leads to the transfer function

$$\frac{i_{gq}^{e}}{i_{gq}^{e*}} = \frac{\frac{K}{L_g}\left(s + \frac{1}{\tau}\right)}{s^2 + \frac{(R+K)}{L_g}s + \frac{K}{L_g\tau}} \tag{C.53}$$

The system has one zero at

$$s_z = -\frac{1}{\tau} \tag{C.54}$$

The system has two poles located at

$$s_{p1,2} = \frac{-\left(\frac{R+K}{L_g}\right) \pm \sqrt{\frac{R^2+2RK+K^2}{L_g^2} - \frac{4K}{L_g\tau}}}{2} \tag{C.55}$$

When the radicand equals zero, the system will have roots with negative real part and zero imaginary part. Thus, the system is critically damped, and the poles will be located at

$$s_{p1,2} = \frac{-R-K}{2L_g} \tag{C.56}$$

The center of the poles are placed with parameter K

$$K = -R - 2L_g s_{p1,2}. \tag{C.57}$$

Parameter τ is chosen to satisfy the condition of the radicand equaling zero, so

$$\tau = \frac{4KL_g}{(R+K)^2}. \tag{C.58}$$

The amount of damping can be adjusted by multiplying τ by a factor of c. When $c < 1$ the system will be underdamped; the radicand is negative and the roots will have an imaginary component. When $c > 1$ the system will be overdamped; the radicand is positive, putting the real part of one root further into the LHP, and the other closer to zero, both by the same amount. After adjusting the damping, the zero is located at

$$s_z = -\frac{1}{c\tau} \tag{C.59}$$

and the poles at

$$s_{p1,2} = \frac{-\left(\frac{R+K}{L_g}\right) \pm \sqrt{\frac{R^2+2RK+K^2}{L_g^2} - \frac{4K}{L_g c\tau}}}{2}. \tag{C.60}$$

C.1.3.2 *d*-Axis Control

The d-axis current controller has the same closed-loop transfer function as the q-axis, except with the d-axis inductance. The d-axis PI controller has parameters similar to the q-axis PI controller.

C.1.4 Reactive Power Control

To regulate the reactive power at the grid terminals, an outer PI control loop is used. The actual reactive power is calculated from the measured grid voltage and current. For the circuit of Fig. C.2, and from (C.20), the actual d-axis current in terms of actual reactive power is

$$i_{gd}^{e} = \frac{2}{3}\left(\frac{Q_g}{v_{gq}^{e}}\right). \tag{C.61}$$

Assuming positive parameters K and τ, the output of the reactive power controller is the d-axis current command, defined as

$$i_{gd}^{e*} = \left(Q_g^* - Q_g\right) K_Q \left(1 + \frac{1}{\tau_Q s}\right). \tag{C.62}$$

Assuming the actual current equals the commanded current, then equating (C.61) and (C.62) in the frequency domain leads to the transfer function

$$\frac{Q_g}{Q_g^*} = \frac{\frac{3v_{gq}^{e}K_Q}{2+3v_{gq}^{e}K_Q}\left(s + \frac{1}{\tau_Q}\right)}{s + \frac{3v_{gq}^{e}K_Q}{2+3v_{gq}^{e}K_Q\tau_Q}}. \tag{C.63}$$

The system has one zero, located at

$$s_{zQ} = -\frac{1}{\tau_Q}. \tag{C.64}$$

Parameter τ_Q is chosen to place the zero, as

$$\tau_Q = \frac{-1}{s_{zQ}}. \tag{C.65}$$

The system has one pole, located at

$$s_{pQ} = \frac{-3v_{gq}^{e}K_Q}{2 + 3v_{gq}^{e}K_Q\tau_Q}. \tag{C.66}$$

Parameter K_Q is chosen to place the pole, as

$$K_Q = \frac{2}{3v_{gq}^{e}\left(\frac{s_{zQ}}{s_{pQ}} - 1\right)}. \tag{C.67}$$

To ensure stability, both the zero and the pole are placed in the LHP [19], [20]. To satisfy $K > 0$, the zero should be placed at a location more negative than the pole, so $s_z < s_p < 0$. The value of v_{gq}^{e} is taken to be V_m.

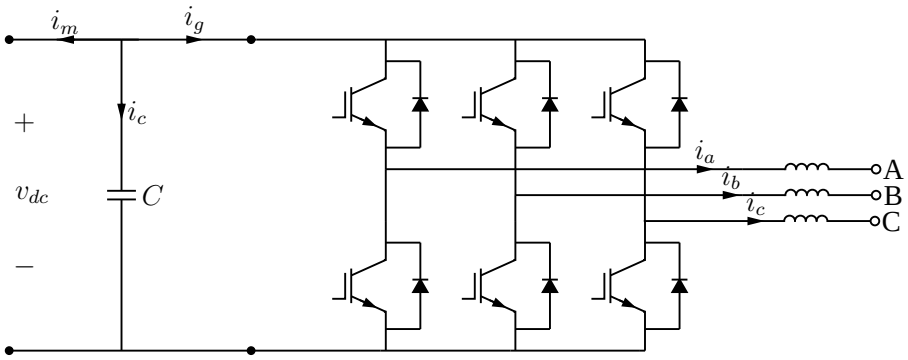

Figure C.4 Circuit diagram of the dc-link and grid-coupled GSC.

C.1.5 DC-Link Voltage Control

The dc-link circuit diagram is in Fig. C.4. The dc-link is initially charged via the grid voltage through the six-switch converter flyback diodes. A PI controller regulates the dc-link voltage to a value sufficiently high enough to allow normal operation of the converter, which entails accommodating changes in the machine-side power.

Because the grid-side current, i_g, is controlled via power electronics, and the machine-side current, i_m, varies with wind power, it is assumed that i_m varies much more slowly than i_g. Therefore, the capacitor current is essentially

$$i_c = C\frac{dv_{dc}}{dt} = -i_g. \tag{C.68}$$

Positive power is defined as out of the converter terminals, and positive capacitor power is defined as into the capacitor. When power is extracted from the grid, it is injected into the capacitor, so

$$-P_g = P_c \tag{C.69}$$

$$-v_{dc}i_g = v_{dc}i_c. \tag{C.70}$$

Assuming no power loss between the dc-link and the grid terminals, then considering the grid terminal power, (C.70) becomes

$$-\frac{3}{2}v_{gq}^e i_{gq}^e = v_{dc}C\frac{dv_{dc}}{dt}. \tag{C.71}$$

Rearranging leads to the grid q-axis current in terms of the dc-link voltage, as

$$i_{gq}^{e} = -\frac{v_{dc} C \frac{dv_{dc}}{dt}}{\frac{3}{2} v_{gq}^{e}}. \tag{C.72}$$

The dc-link voltage is regulated by adjusting the power at the grid terminals. This is accomplished via the q-axis grid current command, defined as

$$i_{gq}^{e*} = -\left(v_{dc}^{*} - v_{dc}\right) K \left(1 + \frac{1}{\tau s}\right). \tag{C.73}$$

Again, parameters K and τ are assumed positive. When the actual dc-link voltage is larger than the commanded voltage, the current command will be increased, extracting more power from the dc-link and thereby reducing the voltage.

Assuming the actual current equals the commanded current, equating (C.72) and (C.73) in the frequency domain yields the transfer function

$$\frac{v_{dc}}{v_{dc}^{*}} = \frac{\frac{K3v_{gq}^{e}}{2Cv_{dc}}\left(s + \frac{1}{\tau}\right)}{s^2 + \frac{K3v_{gq}^{e}}{2Cv_{dc}} s + \frac{K3v_{gq}^{e}}{2Cv_{dc}\tau}}. \tag{C.74}$$

The system has one zero located at

$$s_z = \frac{-1}{\tau} \tag{C.75}$$

and two poles which depend on v_{dc}, located at

$$s_{p1,2} = \frac{\frac{-K3v_{gq}^{e}}{2Cv_{dc}} \pm \sqrt{\left(\frac{K3v_{gq}^{e}}{2Cv_{dc}}\right)^2 - \frac{6Kv_{gq}^{e}}{Cv_{dc}\tau}}}{2}. \tag{C.76}$$

When the radicand equals zero, the poles are strictly real and located at

$$s_{p1,2} = \frac{-3Kv_{gq}^{e}}{4Cv_{dc}}. \tag{C.77}$$

The pole locations depend on the dc-link operating voltage, and gain K. Parameter K is found by

$$K = \frac{-4Cv_{dc}s_{p1,2}}{3v_{gq}^{e}}. \tag{C.78}$$

where v_{dc} is equal to desired operating voltage. Satisfying the condition of the radicand equaling zero leads to the value of τ, as

$$\tau = \frac{8Cv_{dc}}{3v_{gq}^{e}K}. \tag{C.79}$$

The amount of damping can be adjusted with a damping factor, c, multiplying the value of τ. When $c < 1$, the radicand is negative, and the poles have an oscillatory component. When $c > 1$, the radicand is positive, making one pole larger and the other smaller, both by equal amounts. After adjusting the damping, the zero is located at

$$s_z = \frac{-1}{c\tau} \tag{C.80}$$

and the poles are located at

$$s_{p1,2} = \frac{\frac{-K3v_{gq}^e}{2Cv_{dc}} \pm \sqrt{\left(\frac{K3v_{gq}^e}{2Cv_{dc}}\right)^2 - \frac{6Kv_{gq}^e}{Cv_{dc}c\tau}}}{2}. \tag{C.81}$$

C.1.6 Timing And Pole Placement

Through experimentation, the following set of filter corner frequencies and pole/zero relations is obtained to make the controller function satisfactorily.

C.1.6.1 Controller Fundamental Step Size

The fastest fundamental control frequency attainable on the dSPACE controller, for this application, is

$$f_{con} = 10 \text{ kHz}. \tag{C.82}$$

C.1.6.2 Switching Frequency

The switching frequency is limited by the power devices to a maximum value of 12 kHz. The GSC inductance was chosen for a switching frequency between 5 and 10 kHz. Ideally, the controller fundamental frequency is faster than the switching frequency to ensure sufficient filtering without aliasing. However, because the controller step-time is relatively slow, the switching frequency is placed between the fundamental control frequency and its second harmonic. This minimizes output current ripple, while allowing effective control. Placing the switching frequency at $f_{sw} = 7$ kHz results in acceptable performance.

C.1.6.3 PLL

The d-axis voltage is filtered through a first-order low-pass filter to reduce the amount of switching noise present in the measured grid frequency. The filter corner frequency is placed three decades below the switching frequency

$$f_{cvd} = \frac{f_{sw}}{1000} = 7 \text{ Hz}. \tag{C.83}$$

The controller must be slower than the filter response, so the center of the poles is placed at $s_{p\text{PLL}} = -0.4\,(2\pi f_{cvd})$, with a damping factor of $c = 4$. The resulting poles and zeros are positioned at

$$s_{zPLL} = -2.2 \tag{C.84}$$

$$s_{pPLL1} = -2.36 \tag{C.85}$$

$$s_{pPLL2} = -32.83. \tag{C.86}$$

The q- and d-axis voltage outputs are filtered using a first-order low-pass filter with corner frequency at $f_{cvqd} = \frac{f_{sw}}{10000}$. The resulting qd voltages are free of noise and track the fundamental component of the grid voltage.

C.1.6.4 Current Control

The measured abc line currents are transformed to the synchronous reference frame. In the synchronous reference frame, the values are dc in steady-state. A very slow filter is used for feed-forward terms, and a faster filter used for the current comparator, which allows for faster control. The feed-forward filters have corner frequency of

$$f_{c\text{ff}} = \frac{f_{sw}}{1 \times 10^6} = 7 \text{ mHz} \tag{C.87}$$

making the magnitude of high frequency switching noise greatly reduced. The comparator filter has corner frequency of

$$f_{cI\text{comp}} = \frac{f_{sw}}{50} = 140 \text{ Hz}. \tag{C.88}$$

The closed-loop controller is designed to place the poles as fast as possible, while limiting the overshoot in response to a maximum-current step command. However, the controller cannot be faster than the comparator filter. The poles are to be centered at

$$s_{pI} = -0.9\,(2\pi f_{cI\text{comp}}) = -791.7. \tag{C.89}$$

Additional damping of $c = 5$ is added to reduce overshoot and oscillations. Then the zero and poles are located at

$$s_{zI} = -81.4 \tag{C.90}$$

$$s_{pI1} = -83.6 \tag{C.91}$$

$$s_{pI2} = -1499.8. \tag{C.92}$$

C.1.6.5 Reactive Power Control

The measured reactive power is filtered through a first-order low-pass filter before being compared to the commanded value. The filter corner frequency must be placed so the filter response is slower than the inner current control loop response; it is placed at

$$f_{cQ} = \frac{f_{sw}}{200} = 35 \text{ Hz}. \tag{C.93}$$

The controller parameters K and τ are designed by placing the zero and pole independently, while satisfying the constraint $s_z < s_p < 0$. Furthermore, the zero is placed close to the pole to allow a response to higher frequency dynamics. For $s_z << s_p$, the value of K goes to zero, making the controller response too slow. The pole and zero are placed at

$$s_{pQ} = -0.0007\,(2\pi f_{cQ}) = -0.16 \tag{C.94}$$

$$s_{zQ} = 4 s_{pQ} = -0.63. \tag{C.95}$$

C.1.6.6 DC-Link Voltage Control

The dc-link voltage is filtered before being compared to the commanded value. The filter is a first-order low-pass filter, with corner frequency at

$$f_{cDC} = \frac{f_{sw}}{100} = 70 \text{ Hz}. \tag{C.96}$$

The dc-link voltage controller is tuned to respond quickly enough and with enough damping to allow a full power (2500 W) step change, while ensuring the actual dc-link voltage does not exceed specified minimum (300 V) or maximum (400 V) values. This outer-loop controller must be slower than the inner-loop q-axis current controller. The center of the poles is placed at

$$s_{pDC} = 0.07 s_{pI} = -5.5. \tag{C.97}$$

Additional damping of $c = 5$ is added to reduce oscillation. The resulting poles and zeros are located at

$$s_{pDC1} = -0.6 \tag{C.98}$$

$$s_{pDC2} = -10.5 \tag{C.99}$$

$$s_{zDC} = -0.6. \tag{C.100}$$

C.2 Machine-Side Converter

The MSC controller regulates the electromagnetic torque and the reactive power injection at the grid-side terminals. The torque is controlled to match that applied to the turbine via the wind stream. The reactive power is controlled to be 0 VAR at all times; grid reactive power support functions are not implemented in this design. The design presented here is for the rotor-tied configuration; the stator-tied configuration is very similar. The MSC is connected to the stator terminals, and the rotor terminals are connected to the grid. Rotor voltage and current, as well as the stator current and rotor mechanical speed, are measured in real time.

For each configuration, the GSC regulates the dc-link voltage to $V_{\text{dc}} = (1.12)(\sqrt{2}V_{\text{grid}})$, where V_{grid} is the line-to-line rms terminal voltage of the grid. To operate with the same maximum flux density in both configurations, the rated terminal voltage is applied for each. For the rotor-tied configuration, $V_{\text{grid}} = 195$ V and $V_{\text{dc}} = 309$ V. For the stator-tied configuration, $V_{\text{grid}} = 208$ V and $V_{\text{dc}} = 330$ V. The stator-referred grid-tied terminal voltages are identical in each configuration.

Theory regarding the wound-rotor induction machine is detailed in [4], and summarized here. The voltage equations in the arbitrary reference frame, referred to the stator, are

$$\boldsymbol{v}_{qd0s} = \boldsymbol{r}_s \boldsymbol{i}_{qd0s} + \omega \boldsymbol{\lambda}_{dqs} + p\boldsymbol{\lambda}_{qd0s} \tag{C.101}$$

$$\boldsymbol{v}'_{qd0r} = \boldsymbol{r}'_r \boldsymbol{i}'_{qd0r} + (\omega - \omega_r)\, \boldsymbol{\lambda}'_{dqr} + p\boldsymbol{\lambda}'_{qd0r} \tag{C.102}$$

where p is the derivative operator, $\frac{d}{dt}$, and

$$(\boldsymbol{\lambda}_{dqs})^T = \begin{bmatrix} \lambda_{ds} & -\lambda_{qs} & 0 \end{bmatrix} \tag{C.103}$$

$$\left(\boldsymbol{\lambda}'_{dqr}\right)^T = \begin{bmatrix} \lambda'_{dr} & -\lambda'_{qr} & 0 \end{bmatrix} \tag{C.104}$$

The stator and rotor flux linkages are

$$\begin{bmatrix} \boldsymbol{\lambda}_{qd0s} \\ \boldsymbol{\lambda}'_{qd0r} \end{bmatrix} = \begin{bmatrix} \boldsymbol{K}_s \boldsymbol{L}_s \boldsymbol{K}_s^{-1} & \boldsymbol{K}_s \boldsymbol{L}'_{sr} \boldsymbol{K}_r^{-1} \\ \boldsymbol{K}_r \boldsymbol{L}_{sr} \boldsymbol{K}_s^{-1} & \boldsymbol{K}_r \boldsymbol{L}'_r \boldsymbol{K}_r^{-1} \end{bmatrix} \begin{bmatrix} \boldsymbol{i}_{qd0s} \\ \boldsymbol{i}'_{qd0r} \end{bmatrix}. \tag{C.105}$$

Substituing (C.105) into (C.101 – C.104), and expanding yields

$$v_{qs} = r_s i_{qs} + \omega\lambda_{ds} + p\lambda_{qs} \tag{C.106}$$

$$v_{ds} = r_s i_{ds} - \omega\lambda_{qs} + p\lambda_{ds} \tag{C.107}$$

$$v_{0s} = r_s i_{0s} + p\lambda_{0s} \tag{C.108}$$

$$v'_{qr} = r'_r i'_{qr} + (\omega - \omega_r)\,\lambda'_{dr} + p\lambda'_{qr} \tag{C.109}$$

$$v'_{dr} = r'_r i'_{dr} - (\omega - \omega_r)\,\lambda'_{qr} + p\lambda'_{dr} \tag{C.110}$$

$$v'_{0r} = r'_r i'_{0r} + p\lambda'_{0r} \tag{C.111}$$

where

$$\lambda_{qs} = L_{ls} i_{qs} + L_M \left(i_{qs} + i'_{qr}\right) \tag{C.112}$$

$$\lambda_{ds} = L_{ls} i_{ds} + L_M \left(i_{ds} + i'_{dr}\right) \tag{C.113}$$

$$\lambda_{0s} = L_{ls} i_{0s} \tag{C.114}$$

$$\lambda'_{qr} = L'_{lr} i'_{qr} + L_M \left(i_{qs} + i'_{qr}\right) \tag{C.115}$$

$$\lambda'_{dr} = L'_{lr} i'_{dr} + L_M \left(i_{ds} + i'_{dr}\right) \tag{C.116}$$

$$\lambda'_{0r} = L'_{lr} i'_{0r}. \tag{C.117}$$

It is useful to put the stator voltage equations in terms of rotor flux and stator current. The stator current will be controlled, and rotor flux will be included in the feed-forward terms of the controllers. Rearranging (C.112 – C.117) yields the stator q- and d-axis flux in terms of rotor flux and stator current. For λ_{qs}, using (C.115) and (C.112), and rearranging, yields

$$\lambda_{qs} = \left(1 - \frac{L_M^2}{L_s L'_r}\right) L_s i_{qs} + \frac{L_M}{L'_r}\lambda'_{qr} \tag{C.118}$$

where $L_s = (L_{ls} + L_M)$ and $L'_r = (L'_{lr} + L_M)$. For λ_{ds}, using (C.116) and (C.113), and rearranging, yields

$$\lambda_{ds} = \left(1 - \frac{L_M^2}{L_s L'_r}\right) L_s i_{ds} + \frac{L_M}{L'_r}\lambda'_{dr}. \tag{C.119}$$

Substituting (C.118) and (C.119) into (C.106) and (C.107) yields the stator voltage equations in terms of rotor flux and stator current. The q-axis stator voltage is

$$v_{qs} = (r_s i_{qs} + \sigma L_s p i_{qs}) + \left(\omega\sigma L_s i_{ds} + \omega\frac{L_M}{L'_r}\lambda'_{dr} + \frac{L_M}{L'_r}p\lambda'_{qr}\right) \tag{C.120}$$

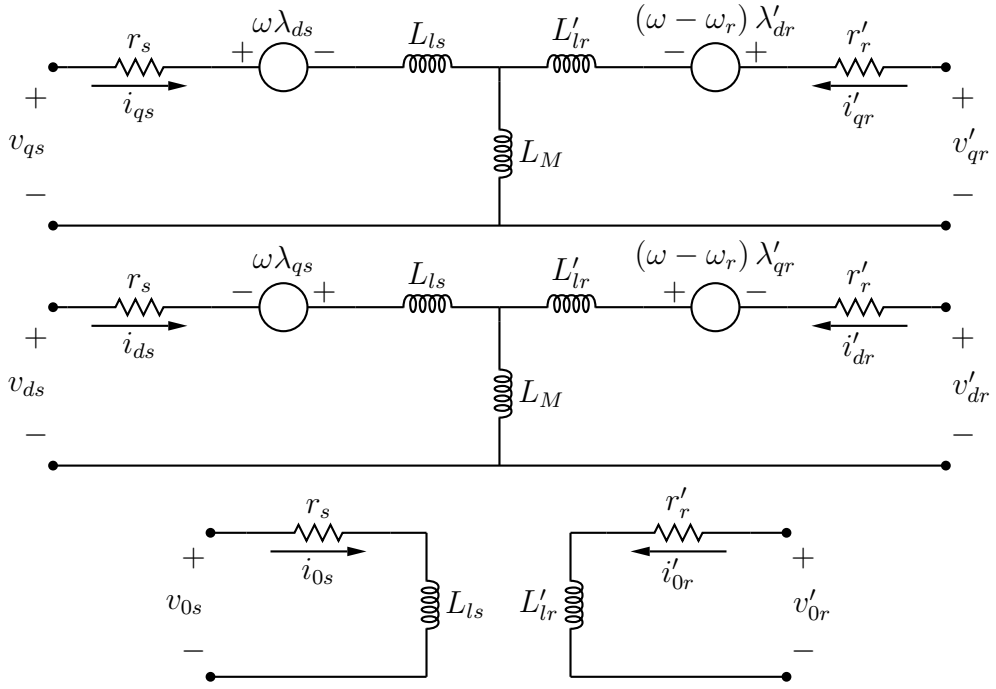

Figure C.5 Dynamic DFIG circuit model in the arbitrary qd reference frame.

where $\sigma = \left(1 - \frac{L_M^2}{L_s L'_r}\right)$. The d-axis stator voltage is

$$v_{ds} = (r_s i_{ds} + \sigma L_s p i_{ds}) + \left(-\omega\sigma L_s i_{qs} - \omega\frac{L_M}{L'_r}\lambda'_{qr} + \frac{L_M}{L'_r}p\lambda'_{dr}\right). \tag{C.121}$$

Voltage equations (C.106) – (C.111) imply the arbitrary qd circuit of Fig. C.5. This circuit has all quantities referred to the stator.

In this model, ω is the angular frequency of the stator currents. The reference frame for which the stator qd voltages have dc values is called the synchronous reference frame, and is labeled ω_e. The speed of the reference frame for which the rotor qd voltages have dc values is $\omega_e - \omega_r$. All control operations are performed in the synchronous reference frame. A PLL measures the grid voltage applied to the rotor terminals. The grid is connected to the machine such that the rotor voltage vector rotates opposite to the direction of the rotor shaft. While connecting the grid in positive sequence, it is necessary to rotate the shaft in the negative direction. Alternatively, the grid voltage could be connected in negative sequence, and the shaft rotate in the positive direction. For this work, the grid terminals are connected to the

machine in positive sequence. In the rotor-tied configuration

$$\omega_e - \omega_r = 2\pi 60 \text{ rad/s}. \tag{C.122}$$

The electrical rotor speed, ω_r, is related to the mechanical rotor speed, ω_{rm}, by

$$\omega_r = \frac{P}{2}\omega_{rm}. \tag{C.123}$$

The slip is defined as

$$s = \frac{\omega_e - \omega_r}{\omega_e}. \tag{C.124}$$

Thus, the angular frequency of electrical quantities in the stator circuit is $\omega_e = 2\pi 60 + \omega_r$ rad/s. The value of ω_r is in the range $[-\pi 60, -3\pi 60]$ rad/s. The angle used in the transformation from synchronous reference frame to the stationary frame, for operation of the stator converter, is

$$\theta_e = (\theta_e - \theta_r) + \theta_r \tag{C.125}$$

where $(\theta_e - \theta_r)$ is measured by the PLL, and θ_r is the electrical shaft angle measured from an absolute encoder.

In the synchronous reference frame, the rotor terminal real and reactive power is

$$P_r = \frac{3}{2}\left(v'^e_{qr} i'^e_{qr} + v'^e_{dr} i'^e_{dr}\right) \tag{C.126}$$

$$Q_r = \frac{3}{2}\left(v'^e_{qr} i'^e_{dr} - v'^e_{dr} i'^e_{qr}\right). \tag{C.127}$$

With the measured grid voltage vector aligned with the q-axis of the synchronous reference frame, $v'^e_{dr} = 0$. This makes the real and reactive power become

$$P_r = \frac{3}{2}\left(v'^e_{qr} i'^e_{qr}\right) \tag{C.128}$$

$$Q_r = \frac{3}{2}\left(v'^e_{qr} i'^e_{dr}\right). \tag{C.129}$$

The controller will use (C.127) to calculate the actual reactive power, for comparison to the commanded value.

The electromagnetic torque developed by the machine, in terms of the currents, is

$$T_e = \left(\frac{3}{2}\right)\left(\frac{P}{2}\right) L_M \left(i^e_{qs} i'^e_{dr} - i^e_{ds} i'^e_{qr}\right) \tag{C.130}$$

which can be written in terms of flux and current as

$$T_e = \left(\frac{3}{2}\right)\left(\frac{P}{2}\right)\left(\lambda^e_{ds} i^e_{qs} - \lambda^e_{qs} i^e_{ds}\right) \tag{C.131}$$

or

$$T_e = \left(\frac{3}{2}\right)\left(\frac{P}{2}\right)\left(\lambda'^e_{qr} i'^e_{dr} - \lambda'^e_{dr} i'^e_{qr}\right). \tag{C.132}$$

Electromagnetic torque is defined positive for accelerating the machine in the positive direction.

The mechanical power applied to the shaft via the wind is [1]

$$P_L = \frac{1}{2}\rho C_p A v_w^3 \tag{C.133}$$

In terms of mechanical rotor speed, ω_{rm}, the torque applied to the shaft via the wind is

$$T_L = \text{sgn}\left(\omega_{rm}\right)\frac{1}{2}\rho C_p A \left(\frac{r}{g\lambda}\right)^3 \omega_{rm}^2 \tag{C.134}$$

and in terms of electrical rotor speed, ω_r, is

$$T_L = \text{sgn}\left(\omega_r\right)\frac{1}{2}\rho C_p A \left(\frac{r}{g\lambda}\right)^3 \left(\frac{2}{P}\omega_r\right)^2 \tag{C.135}$$

where P is the number of poles, $A = \pi r^2$ is the swept area, λ is the tip-speed ratio, g is the gear-ratio, ρ is the air density, and C_p is the performance coefficient. Here, λ is assumed constant. Equation (C.135) can be used to generate the electromagnetic torque command based on measured rotor speed.

C.2.1 Steady-State Operating Point

Based on operating torque and reactive power, the machine will have variable voltages and currents. The rotor d-axis current is determined from (C.129) to be

$$i'^e_{dr} = \frac{2Q_r}{3V'_m}. \tag{C.136}$$

The electrical rotor speed, ω_r, varies with wind speed and is in the range $[-\pi 60, -3\pi 60]$ rad/s. In steady-state, the electromagnetic torque must be $T_e = -T_L$. The rotor q-axis current is found using the electromagnetic torque equation of (C.130)

$$i'^e_{qr} = \frac{\left(\frac{3P}{4}\right) L_M i^e_{qs} i'^e_{dr} - T_e}{\frac{3P}{4} L_M i^e_{ds}}. \tag{C.137}$$

It is useful to put the stator qd currents in terms of rotor d-axis current. For i^e_{qs}, rearranging (C.115)

$$i^e_{qs} = \frac{\lambda'^e_{qr} - L'_r i'^e_{qr}}{L_M} \tag{C.138}$$

and using (C.110)

$$\lambda'^e_{qr} = \frac{-r'_r i'^e_{dr}}{-(\omega_e - \omega_r)} \tag{C.139}$$

leads to

$$i^e_{qs} = \frac{\left(\frac{r'_r i'^e_{dr}}{(\omega_e - \omega_r)}\right) - L'_r i'^e_{qr}}{L_M}. \tag{C.140}$$

For i^e_{ds}, rearranging (C.116)

$$i^e_{ds} = \frac{\lambda'^e_{dr} - L'_r i'^e_{dr}}{L_M} \tag{C.141}$$

and using (C.109)

$$\lambda'^e_{dr} = \frac{v'^e_{qr} - r'_r i'^e_{qr}}{(\omega_e - \omega_r)} \tag{C.142}$$

leads to

$$i^e_{ds} = \frac{\left(\frac{v'^e_{qr} - r'_r i'^e_{qr}}{(\omega_e - \omega_r)}\right) - L'_r i'^e_{dr}}{L_M}. \tag{C.143}$$

Substituting (C.140) and (C.143) into (C.137) yields

$$\frac{3P v'^e_{qr}}{\omega_e - \omega_r} i'^e_{qr} - \frac{3P r'_r}{(\omega_e - \omega_r)} i'^{e2}_{qr} = \frac{3P r'_r i'^{e2}_{dr}}{(\omega_e - \omega_r)} - 4T_e \tag{C.144}$$

and then substituting (C.136) for i'^e_{dr}

$$i'^{e2}_{qr} - \frac{v'^e_{qr}}{r'_r} i'^e_{qr} + \frac{4Q_r^2}{9V_m'^2} - \frac{4T_e(\omega_e - \omega_r)}{3P r'_r} = 0 \tag{C.145}$$

Therefore, the rotor q-axis current is

$$i'^e_{qr1,2} = \frac{\frac{v'^e_{qr}}{r'_r} \pm \sqrt{\left(\frac{v'^e_{qr}}{r'_r}\right)^2 - 4\left(\frac{4Q_r^2}{9v'^{e2}_{qr}} - \frac{4T_e(\omega_e - \omega_r)}{3P r'_r}\right)}}{2}. \tag{C.146}$$

The positive square root term yields an unrealistic result.

The stator q-axis current is determined by rearranging (C.115)

$$i_{qs}^{e} = \frac{\lambda_{qr}'^{e}}{L_M} - \frac{i_{qr}'^{e} L_r'}{L_M} \tag{C.147}$$

where, from (C.110) in steady-state,

$$\lambda_{qr}'^{e} = \frac{v_{dr}'^{e} - r_r' i_{dr}'^{e}}{-(\omega_e - \omega_r)}. \tag{C.148}$$

So substituting yields,

$$i_{qs}^{e} = \frac{v_{dr}'^{e} - r_r' i_{dr}'^{e}}{-(\omega_e - \omega_r) L_M} - \frac{i_{qr}'^{e} L_r'}{L_M}. \tag{C.149}$$

The stator d-axis current is determined by rearranging (C.116)

$$i_{ds}^{e} = \frac{\lambda_{dr}'^{e}}{L_M} - \frac{i_{dr}'^{e} L_r'}{L_M} \tag{C.150}$$

where, from (C.109) in steady-state,

$$\lambda_{dr}'^{e} = \frac{v_{qr}'^{e} - r_r' i_{qr}'^{e}}{(\omega_e - \omega_r)}. \tag{C.151}$$

So substituting yields

$$i_{ds}^{e} = \frac{\left(V_m' - r_r' i_{qr}'^{e}\right)}{(\omega_e - \omega_r) L_M} - \frac{i_{dr}'^{e} L_r'}{L_M}. \tag{C.152}$$

These voltages and currents correspond to given values of rotor reactive power and electromagnetic torque. The fluxes and voltages can be calculated from (C.106) – (C.117).

C.2.2 Phase-Locked Loop

The same PLL design is used for the MSC as was used for the GSC. Although the design is not repeated here, it is important to note that the voltage vector magnitude used in the design is the grid voltage applied to the rotor, after referral to the stator, V_m'. The speed of the reference frame measured by the PLL is $(\omega_e - \omega_r) = 2\pi 60$ rad/s.

C.2.3 Flux Estimator

Machine fluxes are estimated based on measured currents and machine parameters. The flux estimator implements equations (C.112) – (C.117). These equations are repeated here in

the synchronous reference frame (0-axis ignored).

$$\lambda^e_{qs} = L_{ls} i^e_{qs} + L_M \left(i^e_{qs} + i'^e_{qr} \right) \tag{C.153}$$

$$\lambda^e_{ds} = L_{ls} i^e_{ds} + L_M \left(i^e_{ds} + i'^e_{dr} \right) \tag{C.154}$$

$$\lambda'^e_{qr} = L'_{lr} i'^e_{qr} + L_M \left(i^e_{qs} + i'^e_{qr} \right) \tag{C.155}$$

$$\lambda'^e_{dr} = L'_{lr} i'^e_{dr} + L_M \left(i^e_{ds} + i'^e_{dr} \right). \tag{C.156}$$

C.2.4 Stator Current Vector Control

The stator current controller is a PI controller. The outputs of the controller are the q- and d-axis stator voltage commands, in the synchronous reference frame. The angle of (C.125) is used in the transformation from synchronous to stationary reference frames.

C.2.4.1 q-Axis Control

Voltage equation (C.120) relates the stator q-axis current to the stator q-axis voltage; it is restated here for the synchronous reference frame

$$v^e_{qs} = \left(r_s i^e_{qs} + \sigma L_s p i^e_{qs} \right) + \left(\omega_e \sigma L_s i^e_{ds} + \omega_e \frac{L_M}{L'_r} \lambda'^e_{dr} + \frac{L_M}{L'_r} p \lambda'^e_{qr} \right) \tag{C.157}$$

where $\sigma = \left(1 - \frac{L_M^2}{L_s L'_r} \right)$. The voltage command generated by the controller is defined to be

$$v^{e*}_{qs} = \left(i^{e*}_{qs} - i^e_{qs} \right) K \left(1 + \frac{1}{\tau s} \right) + \left(\omega_e \sigma L_s i^e_{ds} + \omega_e \frac{L_M}{L'_r} \lambda'^e_{dr} + \frac{L_M}{L'_r} p \lambda'^e_{qr} \right) \tag{C.158}$$

where $p\lambda'^e_{qr}$ is obtained from (C.109) as

$$p\lambda'^e_{qr} = v'^e_{qr} - r'_r i'^e_{qr} - (\omega_e - \omega_r) \lambda'^e_{dr} \tag{C.159}$$

and the value of λ'^e_{dr} is obtained from (C.156). Assuming the actual voltage created by the converter matches the commanded value, then (C.157) equals (C.158)

$$\left(r_s i^e_{qs} + \sigma L_s p i^e_{qs} \right) + \left(\omega_e \sigma L_s i^e_{ds} + \omega_e \frac{L_M}{L'_r} \lambda'^e_{dr} + \frac{L_M}{L'_r} p \lambda'^e_{qr} \right) =$$
$$= \left(i^{e*}_{qs} - i^e_{qs} \right) K \left(1 + \frac{1}{\tau s} \right) + \left(\omega_e \sigma L_s i^e_{ds} + \omega_e \frac{L_M}{L'_r} \lambda'^e_{dr} + \frac{L_M}{L'_r} p \lambda'^e_{qr} \right). \tag{C.160}$$

Rearranging in the frequency domain leads to the transfer function

$$\frac{i_{qs}^{e}}{i_{qs}^{e*}} = \frac{\frac{K}{\sigma L_s}\left(s + \frac{1}{\tau}\right)}{s^2 + \frac{(r_s+K)}{\sigma L_s}s + \frac{K}{\sigma L_s \tau}}. \tag{C.161}$$

The system has one zero located at

$$s_z = \frac{-1}{\tau}. \tag{C.162}$$

The system has two poles located at

$$s_{p1,2} = \frac{-\frac{(r_s+K)}{\sigma L_s} \pm \sqrt{\left(\frac{(r_s+K)}{\sigma L_s}\right)^2 - \frac{4K}{\sigma L_s \tau}}}{2}. \tag{C.163}$$

When the radicand equals zero, the poles are both located at

$$s_{p1,2} = -\left(\frac{r_s + K}{2\sigma L_s}\right). \tag{C.164}$$

The center of the poles can be placed by choosing the value of K to be

$$K = -2\sigma L_s s_{p1,2} - r_s. \tag{C.165}$$

Making the radicand equal zero yields parameter τ, as

$$\tau = \frac{4K\sigma L_s}{(r_s + K)^2}. \tag{C.166}$$

Additional damping can be added to the system by multiplying τ by a constant, c. For $c < 1$, the radicand is negative, giving the poles an imaginary component. For $c > 1$, the radicand is positive, making one pole larger and one pole smaller, both by equal amounts. After adjusting the damping, the zero is located at

$$s_z = \frac{-1}{c\tau} \tag{C.167}$$

and the poles are located at

$$s_{p1,2} = \frac{-\frac{(r_s+K)}{\sigma L_s} \pm \sqrt{\left(\frac{(r_s+K)}{\sigma L_s}\right)^2 - \frac{4K}{\sigma L_s c\tau}}}{2}. \tag{C.168}$$

C.2.4.2 *d*-Axis Control

Voltage equation (C.121) relates the stator d-axis current to the stator d-axis voltage; it is restated here for the synchronous reference frame

$$v_{ds}^{e} = \left(r_s i_{ds}^{e} + \sigma L_s p i_{ds}^{e}\right) + \left(-\omega_e \sigma L_s i_{qs}^{e} - \omega_e \frac{L_M}{L_r'} \lambda_{qr}'^{e} + \frac{L_M}{L_r'} p\lambda_{dr}'^{e}\right) \tag{C.169}$$

where $\sigma = \left(1 - \frac{L_M^2}{L_s L_r'}\right)$. The voltage command generated by the controller is defined to be

$$v_{ds}^{e*} = \left(i_{ds}^{e*} - i_{ds}^{e}\right) K \left(1 + \frac{1}{\tau s}\right) + \left(-\omega_e \sigma L_s i_{qs}^{e} - \omega_e \frac{L_M}{L_r'} \lambda_{qr}'^{e} + \frac{L_M}{L_r'} p\lambda_{dr}'^{e}\right) \tag{C.170}$$

where $p\lambda_{dr}'^{e}$ is obtained from (C.110) as

$$p\lambda_{dr}'^{e} = v_{dr}'^{e} - r_r' i_{dr}'^{e} + \left(\omega_e - \omega_r\right) \lambda_{qr}'^{e} \tag{C.171}$$

and the value of $\lambda_{qr}'^{e}$ is obtained from (C.155). Assuming the actual voltage created by the converter matches the commanded value, then (C.169) equals (C.170)

$$\begin{aligned}\left(r_s i_{ds}^{e} + \sigma L_s p i_{ds}^{e}\right) + \left(-\omega_e \sigma L_s i_{qs}^{e} - \omega_e \frac{L_M}{L_r'} \lambda_{qr}'^{e} + \frac{L_M}{L_r'} p\lambda_{dr}'^{e}\right) = \\ = \left(i_{ds}^{e*} - i_{ds}^{e}\right) K \left(1 + \frac{1}{\tau s}\right) + \left(-\omega_e \sigma L_s i_{qs}^{e} - \omega_e \frac{L_M}{L_r'} \lambda_{qr}'^{e} + \frac{L_M}{L_r'} p\lambda_{dr}'^{e}\right).\end{aligned} \tag{C.172}$$

Rearranging in the frequency domain leads to the closed-loop transfer function

$$\frac{i_{ds}^{e}}{i_{ds}^{e*}} = \frac{\frac{K}{\sigma L_s}\left(s + \frac{1}{\tau}\right)}{s^2 + \frac{(r_s + K)}{\sigma L_s} s + \frac{K}{\sigma L_s \tau}}. \tag{C.173}$$

This is the same transfer function as was found for the q-axis current controller. The d-axis controller will have the same control parameters as the q-axis.

C.2.5 Rotor Reactive Power Control

The reactive power controller is a PI controller. The output is the d-axis stator current command in the synchronous reference frame. Substituting (C.116) into (C.129) yields

$$Q_r = \frac{3}{2}\left(\frac{v_{qr}'^{e} \lambda_{dr}'^{e}}{L_r'} - \frac{v_{qr}'^{e} L_M i_{ds}^{e}}{L_r'}\right). \tag{C.174}$$

Rearranging leads to the d-axis stator current in terms of rotor reactive power

$$i_{ds}^{e} = \left(\frac{\lambda_{dr}'^{e}}{L_M}\right) - \frac{2}{3}\left(\frac{Q_r L_r'}{v_{qr}'^{e} L_M}\right). \tag{C.175}$$

Assuming positive gain parameters K and τ, the d-axis stator current command is defined to be

$$i_{ds}^{e*} = \left(\frac{\lambda_{dr}'^{e}}{L_M}\right) + (Q_r - Q_r^*) K \left(1 + \frac{1}{\tau s}\right). \tag{C.176}$$

Assuming the controller makes the actual reactive power equal the commanded value, then it follows that (C.175) equals (C.176). Rearranging in the frequency domain yields the transfer function

$$\frac{Q_r}{Q_r^*} = \frac{K\left(s + \frac{1}{\tau}\right)}{\left(\frac{2L_r'}{3v_{qr}'^{e} L_M} + K\right) s + \frac{K}{\tau}}. \tag{C.177}$$

The system has one zero located at

$$s_z = \frac{-1}{\tau} \tag{C.178}$$

and one pole located at

$$s_p = \frac{-1}{\left(\frac{2L_r'}{3v_{qr}'^{e} L_M K} + 1\right)\tau}. \tag{C.179}$$

The value of τ can be determined by placing the zero at a specific location, as

$$\tau = \frac{-1}{s_z} \tag{C.180}$$

The value of K can be determined by placing the pole at a specific location, as

$$K = \frac{2L_r'\left(\frac{s_p}{s_z}\right)}{3v_{qr}'^{e} L_M\left(1 - \left(\frac{s_p}{s_z}\right)\right)}. \tag{C.181}$$

Both the zero and the pole are placed in the left half plane. To satisfy $K > 0$, it is necessary that $|s_z| > |s_p|$; the zero must be more negative than the pole.

C.2.6 Electromagnetic Torque Control

Electromagnetic torque is controlled via a PI controller. The output of the controller is the stator q-axis current command, in the synchronous reference frame. It is necessary to relate the

torque to the stator q-axis current Equation (C.132) is manipulated to relate torque to stator current, and is restated here

$$T_e = \left(\frac{3}{2}\right)\left(\frac{P}{2}\right)\left(\lambda'^e_{qr} i'^e_{dr} - \lambda'^e_{dr} i'^e_{qr}\right). \tag{C.182}$$

Rearranging (C.115) and substituting for i'^e_{qr}, and rearranging (C.116) for i'^e_{dr}, the torque equation becomes

$$T_e = \left(\frac{3}{2}\right)\left(\frac{P}{2}\right)\left(\frac{L_M}{L'_r}\right)\left(-\lambda'^e_{qr} i^e_{ds} + \lambda'^e_{dr} i^e_{qs}\right). \tag{C.183}$$

Rearranging leads to the stator q-axis current in terms of torque

$$i^e_{qs} = \frac{\lambda'^e_{qr} i^e_{ds}}{\lambda'^e_{dr}} + \left(\frac{4T_e L'_r}{3PL_M \lambda'^e_{dr}}\right). \tag{C.184}$$

The incoming wind stream provides negative torque, making the rotor spin in the negative direction. Therefore, generator torque is commanded positive. The q-axis stator current command is defined to be

$$i^{e*}_{qs} = \frac{\lambda'^e_{qr} i^e_{ds}}{\lambda'^e_{dr}} + \left(T^*_e - T_e\right) K \left(1 + \frac{1}{\tau s}\right). \tag{C.185}$$

The controller works to make the actual current equal the desired current. Equating (C.184) and (C.185), rearranging in the frequency domain leads to the transfer function

$$\frac{T_e}{T^*_e} = \frac{\frac{K3PL_M\lambda'^e_{dr}}{\left(4L'_r + K3PL_M\lambda'^e_{dr}\right)}\left(s + \frac{1}{\tau}\right)}{s + \frac{K3PL_M\lambda'^e_{dr}}{\left(4L'_r + K3PL_M\lambda'^e_{dr}\right)\tau}}. \tag{C.186}$$

The system has one zero located at

$$s_z = \frac{-1}{\tau} \tag{C.187}$$

and one pole located at

$$s_p = \frac{-K3PL_M\lambda'^e_{dr}}{\left(4L'_r + K3PL_M\lambda'^e_{dr}\right)\tau}. \tag{C.188}$$

The zero can be placed at a specific location by choosing τ to be

$$\tau = \frac{-1}{s_z}. \tag{C.189}$$

The pole can be placed at a specific location by choosing K to be

$$K = \frac{4L'_r \left(\frac{s_p}{s_z}\right)}{3PL_M \lambda'^e_{dr} \left(1 - \frac{s_p}{s_z}\right)}. \tag{C.190}$$

From (C.109) in steady-state, $\lambda'^e_{dr} \approx \frac{v'^e_{qr}}{\omega_e - \omega_r}$, so

$$K = \frac{4L'_r \left(\omega_e - \omega_r\right) \left(\frac{s_p}{s_z}\right)}{3PL_M V'^e_{qr} \left(1 - \frac{s_p}{s_z}\right)}. \tag{C.191}$$

Nominally, $v'^e_{qr} = V'_m$ and $(\omega_e - \omega_r) = 2\pi 60$ rad/s. Both the pole and the zero are placed in the left half plane. To ensure $K > 0$, it is necessary to place the poles and zeros such that $\frac{s_p}{s_z} < 1$, so $|s_p| < |s_z|$; the zero should be more negative than the pole.

C.2.7 Timing And Pole Placement

C.2.7.1 Controller Fundamental Step Size

The controller used is a d-SPACE DS1103. The controller fundamental step size is set to be as fast as possible, while still being able to run the real-time interface. The fundamental step size is 100 μs, resulting in a control frequency of 10 kHz..

C.2.7.2 Switching Frequency

The power electronic switching frequency is chosen to be $f_{sw} = 7$ kHz. Increasing to 10 kHz results in aliased sampling of the voltage and current by the ADC, due to switching noise; this also happens at 5 kHz. Lower switching frequencies, such as 1 kHz and 3 kHz, results in switching noise with higher magnitude, thus requiring additional filtering, effectively slowing down the controller. Choosing 7 kHz results in the best performance.

C.2.7.3 PLL

The PLL is designed to have the d-axis voltage filtered with a first-order low-pass filter with corner frequency at $f_{cvd} = \frac{f_{sw}}{1000}$. The controller is designed to have the central pole location placed at $s_{pPLL} = -(0.4)(2\pi f_{cvd})$, with a damping coefficient of $c = 4$. The resulting poles

and zeros are positioned at

$$s_{zPLL} = -2.2 \tag{C.192}$$

$$s_{pPLL1} = -2.36 \tag{C.193}$$

$$s_{pPLL2} = -32.83. \tag{C.194}$$

The q- and d-axis voltage outputs are filtered using a first-order low-pass filter with corner frequency at $f_{cvqd} = \frac{f_{sw}}{10000}$. The resulting qd voltages are free of noise and track the fundamental component of the grid voltage.

C.2.7.4 Current Control

The measured abc line currents are measured and transformed to the synchronous reference frame, in which the values are dc in steady-state. Feed forward terms are filtered with $f_{c\text{ff}} = \frac{f_{sw}}{1\times10^6}$. This very slow filter is required to attenuate the switching, SVM, and machine harmonics. A first-order low-pass filter with corner frequency of $f_{cI\text{comp}} = \frac{f_{sw}}{50}$ is used to filter the actual current measurement, before it is compared to the commanded value. The controller's central pole location is placed relatively close to the corner frequency of the comparator filter to make the controller fast enough to generate a sinusoidal current having maximum frequency of $\pm$30 Hz. Because the controller fundamental frequency is only 10 kHz, the controller will not be able to eliminate current harmonics at frequencies above this value, such as those caused by machine slots and SVM. The poles are placed at

$$s_{pI} = -0.9\,(2\pi f_{cI\text{comp}}) = -79.2 \tag{C.195}$$

and additional damping of $c = 5$ is used to reduce overshoot and oscillation. The resulting poles and zero are located at

$$s_{zI} = -81.4 \tag{C.196}$$

$$s_{pI1} = -83.6 \tag{C.197}$$

$$s_{pI2} = -1499.8. \tag{C.198}$$

C.2.7.5 Reactive Power Control

The measured reactive power is filtered through a first-order low-pass filter before being compared with the commanded value. This filter must have a response that is slower than the inner current control loop; the corner frequency is placed at

$$f_{cQ} = \frac{f_{sw}}{5000} = 1.4 \text{ Hz}. \tag{C.199}$$

Control parameters K and τ are designed by placing the zero and pole independently, while satisfying the constraint $s_z < s_p < 0$. The zero is placed close to the pole to allow a response to higher frequency dynamics. The pole and zero are placed at

$$s_{pQ} = -0.5\,(2\pi f_{cQ}) = -4.4 \tag{C.200}$$

$$s_{zQ} = 2s_{pQ} = -8.8. \tag{C.201}$$

C.2.7.6 Torque Control

The measured torque is filtered through a first-order low-pass filter before being compared to the commanded value. The corner frequency of this filter is at

$$f_{cT} = \frac{f_{sw}}{5000} = 1.4 \text{ Hz}. \tag{C.202}$$

Feed forward terms are filtered to eliminate switching noise and other harmonics. This is also a first-order low-pass filter with corner frequency at

$$f_{cT\text{comp}} = \frac{f_{sw}}{1 \times 10^6} = 7 \text{ mHz}. \tag{C.203}$$

The controller poles are placed such that the controller response is slower than the comparator filter response. Also, the zero is placed near the pole to allow a response to higher frequency dynamics. The pole and zero are placed at

$$s_{pT} = -0.5\,(2\pi f_{cT\text{comp}}) = -4.4 \tag{C.204}$$

$$s_{zT} = 2s_{pT} = -8.8. \tag{C.205}$$

C.2.8 Pre-Enabled Steady-State Condition

In this design, the machine is initially magnetized by the grid. To activate the controller with minimal impact on torque and reactive power, the controller outputs must be initialized. Before enabling the controller, the sum of the feed-forward terms and the initial value of the integrator must be equal to the pre-enabled condition.

The steady-state rotor voltage measured by the PLL is $v'^{e}_{dr} = 0$ and $v'^{e}_{qr} = V'_m$. From (C.109) and (C.110), along with (C.115) and (C.116)

$$0 = r'_r i'^{e}_{dr} - (\omega_e - \omega_r)\left(L'_r i'^{e}_{qr} + L_M i^{e}_{qs}\right). \tag{C.206}$$

With the stator open-circuited, this becomes

$$0 = r'_r i'^{e}_{dr} - (\omega_e - \omega_r)\left(L'_r i'^{e}_{qr}\right). \tag{C.207}$$

Then

$$i'^{e}_{dr} = \frac{(\omega_e - \omega_r) L'_r i'^{e}_{qr}}{r'_r} \tag{C.208}$$

and

$$i'^{e}_{qr} = \frac{V'_m r'_r}{\left(r'^{2}_r + (\omega_e - \omega_r)^2 L'^{2}_r\right)}. \tag{C.209}$$

The reactive power is then easily calculated from (C.127). The stator qd voltage during the pre-enabled state, with the convert not activated, is

$$v^{e}_{qs} = \omega_e L_M i'^{e}_{dr} \tag{C.210}$$

$$v^{e}_{ds} = -\omega_e L_M i'^{e}_{qr}. \tag{C.211}$$

When testing the controller, the initial output of the integrator can be tuned to obtain these values.

C.2.9 Dynamometer Speed Control

The dynamometer controls the speed of the shaft using a PI controller. The output of the controller is a mechanical torque reference command, derived from the speed error. The

mechanical shaft torque, T_m, (provided by the dynamometer) is related to the shaft speed by the swing equation

$$J\frac{d}{dt}\omega_{rm} = T_e - T_m. \tag{C.212}$$

where J is the inertia of the shaft, ω_{rm} is the mechanical rotor speed, and T_e is the electromagnetic torque of the DFIG. The actual mechanical torque is therefore

$$T_m = T_e - J\frac{d}{dt}\omega_{rm}. \tag{C.213}$$

The desired mechanical torque command is defined to be

$$T_m^* = T_e + K\left(1 + \frac{1}{\tau s}\right)\left(\omega_{rm} - \omega_{rm}^*\right). \tag{C.214}$$

Assuming the controller makes the actual torque equal the commanded, then equating (C.213) and (C.214), and rearranging in the frequency domain yields the transfer function

$$\frac{\omega_{rm}}{\omega_{rm}^*} = \frac{\frac{K}{J}\left(s + \frac{1}{\tau}\right)}{s^2 + \frac{K}{J}s + \frac{K}{J\tau}}. \tag{C.215}$$

The system has one zero located at

$$s_z = \frac{-1}{\tau} \tag{C.216}$$

and two poles located at

$$s_{p1,2} = \frac{-\frac{K}{J} \pm \sqrt{\frac{K^2}{J^2} - \frac{4K}{J\tau}}}{2}. \tag{C.217}$$

When the radicand equals zero, the poles are both located at

$$s_{p1,2} = -\frac{K}{2J}. \tag{C.218}$$

The center of the poles can be placed by choosing the value of K to be

$$K = -2Js_{p1,2}. \tag{C.219}$$

Setting the radicand equal to zero yields parameter τ

$$\tau = \frac{4J}{K}. \tag{C.220}$$

Additional damping can be added to the system by multiplying τ by a constant c. For $c < 1$, the radicand is negative, giving the poles an imaginary component. For $c > 1$, the radicand is positive, making one pole larger and one pole smaller, both by equal amounts. After adjusting the damping, the zero is located at

$$s_z = \frac{-1}{c\tau} \tag{C.221}$$

and the poles are located at

$$s_{p1,2} = \frac{-\frac{K}{J} \pm \sqrt{\left(\frac{K}{J}\right)^2 - \frac{4K}{Jc\tau}}}{2}. \tag{C.222}$$

C.2.9.1 Note on Damping

While including the damping coefficient, c, the denominator of the transfer function can be written as

$$s^2 + \frac{K}{J}s + \frac{K}{Jc\tau} = s^2 + 2\zeta\omega_n s + \omega_n^2 \tag{C.223}$$

where ω_n is the natural frequency and ζ is the damping factor. Here, it is apparent that $4\zeta^2\omega_n^2 = \frac{K^2}{J^2}$ and $\omega_n^2 = \frac{K}{Jc\tau}$, which reduces to

$$\zeta^2 = c. \tag{C.224}$$

The method of placing the center of the poles and then set the damping coefficient, c, is similar to the method of setting the natural frequency and damping factor ζ.

APPENDIX D. EXPERIMENT SETUP

Due to the sensitivity of these measurements, it is important to take precise and consistent measurements. The information provided here is presented to show the level of quality aimed for in performing these experiments.

The DFIG shaft is coupled to a DyneSystems Inter-Loc V dynamometer via a flexible coupling, and the machine is aligned to eliminate vibrations. The dynamometer provides torque to the shaft, and is operated in constant speed control mode. Both the GSC and MSC use a Semikron SKS-32F-B6U-E1CIF-B6CI-12-V06 power electronic converter. They are coupled by a 188-μF dc-link. The MSC and GSC are controlled by separate dSPACE DS1103 microcontrollers. Voltages and currents are measured with LEM LV25-P and LA55-P sensors. Rotor speed and position are measured with a BEI HS35F 11-bit absolute encoder. These measurements, along with control signals, are conditioned and interfaced with the controller via a custom circuit board.

The torque sensor was calibrated using the 2-sided span method. Input power was measured using a Tektronix DPO4034B oscilloscope with Tektronix THDP0200 differential voltage probes to capture the dynamometer torque and speed. These measurements were calibrated by removing the dc-offset and tuning the output signal gain. A Tektronix A622 current probe was used to capture line current. Power quality measurements were obtained with a Voltech PM6000 power analyzer connected at the machine terminals. It was configured for PWM mode with an appropriate fundamental frequency, with power measurements made using the two watt-meter method. The oscilloscope and power analyzer captured data simultaneously.

APPENDIX E. TRANSFORMATION PROOFS

E.1 Real And Reactive Power In The Synchronous *qd* Reference Frame

Additional details regarding this derivation are available in [4].

The voltage and currents in the circuit are assumed sinusoidal

$$v_{as}(t) = \sqrt{2}V_s \cos(\omega_e t + \theta_v) \tag{E.1}$$

$$i_{as}(t) = \sqrt{2}I_s \cos(\omega_e t + \theta_i). \tag{E.2}$$

Using Euler's formula, the real time varying function is simply the real component of a rotating vector on the real-imaginary plane, as

$$v_{as}(t) = Re\{\sqrt{2}V_s e^{j\omega_e t} e^{j\theta_v}\} \tag{E.3}$$

$$i_{as}(t) = Re\{\sqrt{2}I_s e^{j\omega_e t} e^{j\theta_i}\}. \tag{E.4}$$

Plotting both the real and imaginary components results in a time varying vector. In phasor notation, this is

$$\tilde{V}_{as} = V_s e^{j\theta_v} \tag{E.5}$$

$$\tilde{I}_{as} = I_s e^{j\theta_i}. \tag{E.6}$$

The rotating vectors, at some snapshot in time, have a magnitude and angle. The magnitude of the vectors are $\sqrt{2}|\tilde{V}_{as}|$ and $\sqrt{2}|\tilde{I}_{as}|$. Projecting the vectors onto the synchronous q and d axes results in

$$\sqrt{2}\tilde{V}_{as} = v_q^e - jv_d^e \tag{E.7}$$

$$\sqrt{2}\tilde{I}_{as} = i_q^e - ji_d^e \tag{E.8}$$

which relates the instantaneous qd quantities in the synchronous reference frame, to the phasors in any other reference frame.

Apparent power for the three-phase system is defined as

$$S = 3\tilde{V}_{as}\tilde{I}^{*}_{as}. \tag{E.9}$$

Substituting yields

$$S = \frac{3}{2}\left(v^{e}_{q}i^{e}_{q} + jv^{e}_{q}i^{e}_{d} - jv^{e}_{d}i^{e}_{q} + v^{e}_{d}i^{e}_{d}\right). \tag{E.10}$$

The instantaneous real and reactive power, in the synchronous reference frame, is then

$$P = \frac{3}{2}\left(v^{e}_{q}i^{e}_{q} + v^{e}_{d}i^{e}_{d}\right) \tag{E.11}$$

$$Q = \frac{3}{2}\left(v^{e}_{q}i^{e}_{d} - v^{e}_{d}i^{e}_{q}\right). \tag{E.12}$$

E.2 Filter Reactor Inductance Transformation

Additional details regarding this transformation are available in [4]. For a three-phase inductive element, the voltage across the inductance is

$$v_{abcs} = p\lambda_{abcs} \tag{E.13}$$

where λ_{abcs} is the flux linkage of the inductive element, and p is the time derivative operator $\frac{d}{dt}$. This is transformed as

$$v_{qd0s} = K_s p\left[K_s^{-1}\lambda_{qd0s}\right]. \tag{E.14}$$

Using the chain rule, this becomes

$$v_{qd0s} = K_s p\left[K_s^{-1}\right]\lambda_{qd0s} + K_s K_s^{-1} p\left[\lambda_{qd0s}\right]. \tag{E.15}$$

The derivative is taken on each element of the matrix, so

$$p\left[K_s^{-1}\right] = \omega\begin{bmatrix} -\sin(\theta) & \cos(\theta) & 0 \\ -\sin\left(\theta - \frac{2\pi}{3}\right) & \cos\left(\theta - \frac{2\pi}{3}\right) & 0 \\ -\sin\left(\theta + \frac{2\pi}{3}\right) & \cos\left(\theta + \frac{2\pi}{3}\right) & 0 \end{bmatrix} \tag{E.16}$$

(E.17)

and

$$K_s p\left[K_s^{-1}\right] = \omega \begin{bmatrix} 0 & 1 & 0 \\ -1 & 0 & 0 \\ 0 & 0 & 0 \end{bmatrix} \tag{E.18}$$

which leads to

$$v_{qd0s} = \omega \begin{bmatrix} 0 & 1 & 0 \\ -1 & 0 & 0 \\ 0 & 0 & 0 \end{bmatrix} \lambda_{qd0s} + p\left[\lambda_{qd0s}\right]. \tag{E.19}$$

In component form, these are

$$v_{qs} = \omega\lambda_{ds} + p\lambda_{qs} \tag{E.20}$$

$$v_{ds} = -\omega\lambda_{qs} + p\lambda_{ds} \tag{E.21}$$

$$v_{0s} = p\lambda_{0s}. \tag{E.22}$$

It is easy to see that in a synchronous rotating reference frame, the derivative term drops out during steady-state, leaving only the speed-voltage. During a transient, or in a non-synchronous reference frame, the derivative term is active and adds to the speed voltage.

For a linear magnetic element, the flux linkage is related to the inductance and current by

$$\lambda_{abcs} = L_s i_{abcs} \tag{E.23}$$

which in *qd0* quantities becomes

$$\lambda_{qd0s} = K_s L_s K_s^{-1} i_{qd0s}. \tag{E.24}$$

For the circuit of Fig. C.1, we will assume a three-phase set of line reactors, with all three phases wound onto the same symmetrical core, resulting in a series inductance, L_g, and some amount of magnetic coupling between phases, M_g. It is important to note that the actual reactor is asymmetrical, and thus, mutual inductance between phases is not the same for all combinations. Disregarding this fact,

$$L_s = \begin{bmatrix} L_g & M_g & M_g \\ M_g & L_g & M_g \\ M_g & M_g & L_g \end{bmatrix} \tag{E.25}$$

and

$$K_s L_s K_s^{-1} = \begin{bmatrix} L_g - M_g & 0 & 0 \\ 0 & L_g - M_g & 0 \\ 0 & 0 & L_g + 2M_g \end{bmatrix}. \tag{E.26}$$

The magnetic flux contained in the element, in *qd0* quantities, is then

$$\begin{bmatrix} \lambda_{qs} \\ \lambda_{ds} \\ \lambda_{0s} \end{bmatrix} = \begin{bmatrix} L_g - M_g & 0 & 0 \\ 0 & L_g - M_g & 0 \\ 0 & 0 & L_g + 2M_g \end{bmatrix} \begin{bmatrix} i_{qs} \\ i_{ds} \\ i_{0s} \end{bmatrix}. \tag{E.27}$$

In component form, these are

$$\lambda_{qs} = (L_g - M_g)\, i_{qs} \tag{E.28}$$

$$\lambda_{ds} = (L_g - M_g)\, i_{ds} \tag{E.29}$$

$$\lambda_{0s} = (L_g + 2M_g)\, i_{0s}. \tag{E.30}$$

The q-axis flux depends only on the q-axis current. The d-axis flux depends only on the d-axis current. Thus, the voltage across the inductance, in *qd0* quantities, is

$$v_{qs} = \omega\,(L_g - M_g)\, i_{ds} + p\,[(L_g - M_g)\, i_{qs}] \tag{E.31}$$

$$v_{ds} = -\omega\,(L_g - M_g)\, i_{qs} + p\,[(L_g - M_g)\, i_{ds}] \tag{E.32}$$

$$v_{0s} = p\,(L_g + 2M_g)\, i_{0s}. \tag{E.33}$$

Assuming L_g and M_g are constant, and i_{qs} and i_{ds} are sinusoidal, this can also be written as

$$v_{qs} = \omega\,(L_g - M_g)\, i_{ds} + j\,(\omega_e - \omega)\,(L_g - M_g)\, i_{qs} \tag{E.34}$$

$$v_{ds} = -\omega\,(L_g - M_g)\, i_{qs} + j\,(\omega_e - \omega)\,(L_g - M_g)\, i_{ds} \tag{E.35}$$

$$v_{0s} = p\,(L_g + 2M_g)\, i_{0s} \tag{E.36}$$

where ω_e is the speed of the synchronous frame (i.e. the speed of electrical quantities in the stationary *abc* reference frame), and ω is the speed of the arbitrary reference frame. The term $(\omega_e - \omega)$ is the angular frequency of the electrical quantities in the *qd0* circuit, for all non-synchronous reference frames.

BIBLIOGRAPHY

[1] O. Anaya-Lara, N. Jenkins, J. Ekanayaka, P. Cartwright, and M. Hughes, *Wind Energy Generation Modelling and Control.* John Wiley & Sons, Ltd, 2009.

[2] A. Keyhani, *Design of smart power grid renewable energy systems.* IEEE Press, 2011.

[3] D. C. Jiles, *Introduction to magnetism and magnetic materials.* CRC Press, 1998.

[4] P. C. Krause, O. Wasynczuk, and S. D. Sudhoff, *Analysis of Electric Machinery.* IEEE Press, 1995.

[5] B. Wu, Y. Lang, N. Zargari, and S. Kouro, *Power Conversion and Control of Wind Energy Systems.* John Wiley & Sons, Inc, 2011.

[6] M. Singh and S. Santoso, "Dynamic models for wind turbines and wind power plants," NREL, Tech. Rep., Oct 2011.

[7] "Nonoriented electrical steels," A product data bulletin by AK Steel Corporation, 2007.

[8] Z. Yu and A. Tuzuner, "Wind speed modeling and energy production simulation with Weibull sampling," in *Proc. IEEE Power and Energy Society General Meeting*, July 2008.

[9] E. S. Takle and J. M. Brown, "Note on the use of Weibull statistics to characterize wind-speed data," *J. Appl. Meteor.*, vol. 17, pp. 556–559, 1978.

[10] Y. Chen and P. Pillay, "An improved formula for lamination core loss calculations in machines operating with high frequency and high flux density excitation," in *Proc. 37th Industry Appl. Conf.*, vol. 2, Oct 2002, pp. 759–766.

[11] Y.-M. You, T. A. Lipo, and B.-I. Kwon, "Design and analysis of a novel grid-connected to rotor type doubly fed induction machine," *IEEE Trans. Magn.*, vol. 48, no. 2, pp. 919–922, Feb. 2012.

[12] D. W. Novotny and S. A. Nasar, "High frequency losses in induction motors. Part II," NASA Lewis Research Center, Cleveland, OH, Book, Microform, 1991.

[13] S. Seman, J. Niiranen, S. Kanerva, A. Arkkio, and J. Saitz, "Performance study of a doubly fed wind-power induction generator under network disturbances," *IEEE Trans. Energy Convers.*, vol. 21, no. 4, pp. 883–890, Dec. 2006.

[14] M. Bongiorno and T. Thiringer, "A generic DFIG model for voltage dip ride-through analysis," *IEEE Trans. Energy Conversion*, vol. 28, no. 1, pp. 76–85, Mar 2013.

[15] A product brochure prepared by Vestas Wind Systems A/S, 2012.

[16] N. David and D. Aliprantis, "DFIG with grid-connected rotor for wind energy conversion system," in *Proc. Intern. Electr. Mach. Drives Conf. (IEMDC)*. IEEE, May 2013, pp. 125–130.

[17] "IEEE standard test procedure for polyphase induction motors and generators," *IEEE Std 112-2004 (Revision of IEEE Std 112-1996)*, pp. 1–79.

[18] A. Luna, J. Rocabert, I. Candela, P. Rodriguez, R. Teodorescu, and F. Blaabjerg, "Advanced structures for grid synchronization of power converters in distributed generation applications," in *Energy Conversion Congress and Exposition (ECCE), 2012 IEEE*, Sept 2012, pp. 2769–2776.

[19] C.-T. Chen, *Linear system theory and design*, 3rd ed. Oxford University Press.

[20] H. K. Khalil, *Nonlinear Systems*, 3rd ed. Prentice Hall.